Theoretical and Applied Fracture Mechanics 147 (2026) 105838

Contents lists available at ScienceDirect

Theoretical and Applied Fracture Mechanics

journal homepage: www.elsevier.com/locate/tafmec

XCT-based equivalent defect for assessing the effect of contour-induced defects on fatigue strength of PBF-LB components

Daniel Perghem [a], Lorenzo Rusnati [a], Sascha Senck [b], Stefano Beretta [a,c,*]

[a] Politecnico di Milano, Department of Mechanical Engineering, via La Masa 1, 20156 Milano, Italy
[b] University of Applied Sciences Upper Austria, Selzhammerstraße 23, 4600 Wels, Austria
[c] Auburn University, National Center for Additive Manufacturing Excellence (NCAME), Auburn, Al 36849, USA

ARTICLE INFO

Keywords:
Contour-induced defects
X-ray computed tomography
PBF-LB
Probabilistic fatigue assessment
Virtual machining

ABSTRACT

The fatigue performance of laser powder bed fusion components is critically governed by process-induced defects, whose distribution and morphology are strongly influenced by contouring strategies. In particular, the near-surface region affected by contouring exhibits a distinct defect population in terms of defect size and density. Several studies have shown that surface removal can expose these defects at the surface.

This study investigates the role of contour-induced defects in the fatigue behaviour of additively manufactured components. A contour-informed probabilistic methodology is proposed, integrating X-ray computed tomography for defect characterisation, a virtual machining procedure to simulate material removal, and a fracture mechanics framework to evaluate defect criticality through stress intensity factors. Extreme value statistics are employed to derive equivalent surface defect distributions representative of fatigue-controlling defects.

The proposed workflow shows good agreement with experimental observations for Ti6Al4V and AlSi10Mg specimens, accurately capturing both fatigue life and failure locations. The approach simplifies probabilistic modelling for components and is subsequently applied successfully to a complex engine bracket.

1. Introduction

The widespread adoption of additively manufactured (AMed) components in critical engineering applications remains constrained by the difficulty of achieving reliable fatigue life predictions [1,2]. This is mainly because of the presence of process-induced defects, which significantly affect fatigue performance [1,3,4]. Unlike conventionally manufactured materials, AMed materials exhibit high variability in defect populations [5,6], including volumetric defects, such as lack-of-fusion defects, gas pores, and keyhole defects, as well as surface roughness [3,7], all of which act as preferential crack-initiation sites.

For AMed components, structural fatigue assessment can be carried out using different approaches. Fracture mechanics methods are widely employed, in which defects are treated as equivalent cracks [8–10]. Commonly used approaches include the El-Haddad model [8,9] combined with Murakami's $\sqrt{\text{area}}$ parameter [11,12], as well as R-curve based methodologies [13,14] and fatigue crack growth (FCG) algorithms [15–17]. The inherent variability of defect populations has driven the development of probabilistic frameworks, including extreme value statistics, weakest-link formulations, and Monte Carlo-based simulations [18–21]. In parallel, data-driven approaches based on machine learning have recently been explored to predict fatigue life from microstructural descriptors, defect morphology, and surface condition [22–24]. However, the effectiveness of these approaches depends strongly on the accurate representation of defect populations, whose formation is governed by the local thermal history during processing, and influenced by variations in energy input, scan strategy, and melt pool stability [25–27].

In particular, contouring strategies play a key role in defining the near-surface defect population and its interaction with the free surface. To ensure a smooth surface finish and achieve dimensional accuracy as close as possible to the nominal geometry in net-shape components, contouring strategies are commonly employed in laser powder bed fusion (PBF-LB) processes [28–30]. These strategies typically consist of one or more laser passes along the perimeter of the hatched region for each layer. However, they introduce significant variations in melt pool behaviour and thermal history within the contoured volume [31]. Consequently, the mechanical and microstructural characteristics evolve from the contour to the hatch region in the as-built condition [32]. These differences include: (i) variations in grain refinement and microstructural morphology [30,33,34]; (ii) the

* Corresponding author at: Politecnico di Milano, Department of Mechanical Engineering, via La Masa 1, 20156 Milano, Italy.
E-mail address: stefano.beretta@polimi.it (S. Beretta).

https://doi.org/10.1016/j.tafmec.2026.105838
Received 28 May 2026; Received in revised form 6 July 2026; Accepted 22 July 2026
Available online 8 August 2026

Nomenclature

Acronyms

AM	additive manufacturing
BM	block maxima
EVS	extreme value statistics
FCG	fatigue crack growth
FE	finite element
LEVD	largest extreme value distribution
NDE	non-destructive evaluation
PBF-LB	powder bed fusion – laser beam
POT	peak-over-threshold
SEM	scanning electron microscopy
SIF	stress intensity factor
VM	virtual machining
XCT	X-ray computed tomography

Symbols

a	crack size/semi-axis of defect
b	semi-axis of defect (normal to surface)
c	semi-axis of defect (loading direction)
d	distance from defect centroid to surface
$\bar{d}_{z,c}$	average inter-defect spacing - circumferential
$\bar{d}_{z,l}$	average inter-defect spacing - longitudinal
δ	scale parameter of the LEVD
$\Delta\sigma$	stress range
Δz	minimum spacing between neighbouring defects
f	fraction of internal-contour defects
F, Y	shape factor
h	edge distance of the defect
K	stress intensity factor
λ	location parameter of the LEVD
ρ_v	volumetric defect density
$\rho_{l,c}$	linear defect density - circumferential
$\rho_{l,l}$	linear defect density - longitudinal
R	stress ratio
σ	applied stress
S_0	reference area for block maxima sampling
S_c	component surface area
T	return period
$\sqrt{area}$	defect size from projected area
$\sqrt{area}_{eq}$	equivalent defect size
$\sqrt{area}_{eff}$	square root of the area enclosing the defect and the free surface

presence of residual stresses extending several hundred microns below the surface [34,35]; and (iii) the formation of a population of process-induced defects, predominantly keyhole porosity [36], with a wide range of morphologies, sizes, and spatial distributions. These defects are characterised by higher density and larger sizes within a confined subsurface layer in contoured regions [34,37–39].

Post-processing operations are often required to improve fatigue performance [40] and ensure tight dimensional tolerances for assembly by reducing surface roughness and removing near-surface defects [41]. Among these operations, both surface treatment and material-removal processes play a key role in determining fatigue properties. The beneficial effect of shot peening on fatigue performance has been widely reported [42–44], primarily because of the formation of near-surface regions characterised by compressive residual stresses induced by localised plastic deformation. In contrast, surface material removal introduces an additional critical variable: the depth of material removed. This depth can significantly influence fatigue behaviour by either eliminating detrimental defects or exposing them at the surface [45]. This effect is particularly relevant in the presence of near-surface defect populations, such as those associated with contouring strategies.

The complete removal of subsurface defects, especially those concentrated in the contour region, typically requires substantial material removal [46,47]. For complex geometries, machining is generally restricted to selected critical areas because of accessibility constraints and manufacturing costs [48], while internal or intricate features may remain unprocessed. Electropolishing has demonstrated significant potential in reducing surface roughness in PBF-LB alloys [49]; however, achieving uniform material removal across all regions remains challenging and requires further optimisation. Similarly, chemical-based polishing techniques [50,51] may be limited by fluid accessibility and transport constraints, particularly in complex or lattice structures [52]. As a result, certain regions may remain in the net-shape condition or undergo only limited material removal. Specifically, the thickness of the removed outer layer determines whether internal subsurface defects are completely eliminated or instead exposed at the surface [39,53]. This effect is particularly pronounced in contoured regions, where defects are typically larger and more densely distributed, thereby increasing their role in fatigue crack initiation.

Despite extensive research on defect-based fatigue modelling, the role of contour-induced defects and their impact after surface material removal are not yet adequately captured by existing approaches. In particular, most probabilistic frameworks [54–57] rely on a uniform volumetric defect population and a distribution of surface features, without explicitly accounting for the distinct near-surface defect population generated by contouring or its interaction with post-processing operations such as material removal. As a result, the contribution of contour-induced defects to fatigue failure may be inaccurately represented, especially in component-scale applications.

To overcome these limitations, a contour-informed X-ray computed tomography (XCT)-based workflow is proposed to derive a prospective equivalent defect distribution. The approach integrates XCT for volumetric defect characterisation [58,59] with a virtual machining (VM) procedure, enabling the simulation of material removal, and the reconstruction of the population of contour defects interacting with the surface. Defects are then analysed within a fracture mechanics framework [8–10] to determine their stress intensity factors (SIFs). Extreme value statistics (EVS) are subsequently employed to derive surface-equivalent defect distributions representative of fatigue-critical defects.

The methodology was developed by analysing two case studies involving Ti6Al4V [38] and AlSi10Mg specimens [39], in which contour-induced defects became critical after surface removal. The analysis showed that the equivalent defect distribution could be readily applied to fatigue life estimation in simple geometries. The method also provides a significant simplification for the analysis of a complex jet engine bracket manufactured with the same process of AlSi10Mg specimens.. The results demonstrate that the proposed workflow can accurately reproduce experimental observations and identify the regions governing fatigue failure.

2. Experimental database

2.1. Ti6Al4V specimens

The first dataset analysed consisted of Ti6Al4V fatigue specimens obtained from a previously experimental investigation [38]. The samples were manufactured by PBF-LB using a Renishaw AM500Q system. The adopted scanning strategy comprised two contour scans, offset by 50 μm from each other, with the outer contour shifted by 100 μm from the nominal geometry. The contour scan was completed before bulk hatching in spot melting mode, resulting in a contour region affected by process-induced defects. After fabrication, all specimens were stress-relieved at 650 °C for 2 h followed by furnace cooling to remove residual stresses induced by the printing process.

Fatigue tests were performed under two different surface conditions: (i) net-shape and (ii) Hirtisation®, an electrochemical milling process before testing. The Hirtisation® process removed material to an average radial depth of approximately 66 μm, reducing the maximum roughness peak height by 57% through the elimination of the deep and sharp valleys typical of the as-built condition, and resulting in an areal roughness of S_a = 6.8 μm and S_v = 49.1 μm. All tests were conducted under fully reversed loading, R=-1, using a servo-hydraulic testing system.

Fractographic analyses were performed by scanning electron microscopy (SEM) to identify crack initiation mechanisms. In the net-shape condition, fatigue cracks predominantly initiated from surface irregularities associated with the as-built roughness. Although contour-induced defects were present beneath the surface (Fig. 1(a) and (b)), they did not govern failure, as sharper surface features generated a higher local crack-driving force.

In contrast, the Hirtisation® specimens exhibited a different initiation behaviour. In most specimens, the substantial reduction in surface roughness shifted crack initiation from superficial irregularities to near-surface contour defects located in the subsurface region or exposed at the free surface. As shown in Fig. 1(a) and (b), these contour-induced defects acted as the primary crack initiation sites. This effect occurred because the chemically removed layer was thinner than the depth of the contour-induced defects.

2.2. AlSi10Mg specimens and bracket component

The second dataset comprised AlSi10Mg fatigue specimens analysed in the present study originated from an experimental campaign reported previously [39]. The samples were manufactured by PBF-LB using a custom parameter set optimised to reduce surface roughness through a tailored contouring strategy. Although this approach enhanced surface quality, it promoted the formation of contour-induced keyhole porosity in the near-surface region.

Specimens were printed in pairs and supported by a central column, which was subsequently removed by machining, with approximately 100 μm of the surface layer removed (Fig. 1(d)), resulting in one machined side. After fabrication, stress-relief heat treatment was applied at 200 °C for 2 h. In addition, shot peening with stainless-steel beads was performed on the external surfaces. The net-shape shot-peened surfaces exhibited an areal roughness of S_a = 6.9 μm and S_v = 41.1 μm. High-cycle fatigue tests were conducted under constant-amplitude loading, with a nominal load ratio of R = 0.1, using a servo-hydraulic testing system.

SEM fractography revealed that fatigue failures were primarily controlled by contour-induced defects located at or in close proximity to the free surface on the machined side. In particular, machining exposed pre-existing contour porosity, effectively converting near-surface defects into surface-breaking flaws that acted as the primary crack initiation sites (Fig. 1(c) and (d)). The limited amount of material removed during machining, approximately 100 μm, was insufficient to remove the contour-affected region. Instead of being eliminated, these defects were geometrically intersected by the machined surface, promoting premature crack initiation. These findings indicate that, despite process optimisation aimed at reducing surface roughness, fatigue performance remained controlled by contour-induced defects exposed by post-processing operations that did not fully remove the contour-affected layer.

The same material and processing conditions were adopted for the bracket geometry considered in this work, which was based on a topology-optimised jet engine component (M. Kurniawan, GE Jet Engine Bracket Version 1.2 [60]). The bracket was manufactured via PBF-LB in AlSi10Mg using analogous contouring strategies and post-processing steps, including stress-relief heat treatment and shot peening. The lug regions were subsequently machined, while the main body was retained in the net-shape condition and shot peened [61].

The finite element (FE) results [62], shown in Fig. 2(a), highlight stress concentrations in the lug region of the component. This is consistent with the experimentally observed failure location shown in Fig. 2(b), where crack initiation occurred in a machined area, further supporting the critical role of surface-exposed defects [39].

2.3. XCT

XCT was employed to characterise the defect population in the Ti6Al4V net-shape specimens, the AlSi10Mg specimens, and the engine bracket.

For the Ti6Al4V material, XCT scans were performed on six specimens in the present study. High-resolution acquisitions of the central gauge region were conducted using a Nanotom 180NF system (GE Phoenix) with a voxel size of 5 μm. The main acquisition parameters were an acceleration voltage of 100 kV, a current of 50 μA, 1500 projections, and an exposure time of 800 ms.

XCT datasets for the AlSi10Mg specimens and the bracket were taken from the studies reported in [39,63], respectively. For the bracket, the scan was performed at a voltage of 200 kV and a current of 150 μA, using 1800 projections and an integration time of 4000 ms. For the specimens, a voltage of 150 kV and a current of 150 μA were used, with an integration time of 600 ms and 1500 projections.

Reconstructed volumes were analysed using the porosity/inclusion analysis module of VGStudio Max version 3.4.2. Defect segmentation was performed using the EasyPore algorithm with a relative threshold of approximately 60% for Ti6Al4V and approximately 44% for AlSi10Mg, without applying image filtering. A minimum defect volume of 27 voxels was imposed to eliminate noise-related artefacts.

Several geometrical descriptors were extracted from the segmented volumes, including defect volume, projected area, bounding-box dimensions, and centroid coordinates. Given its relevance to fatigue-critical applications, the Murakami $\sqrt{area}$ parameter [11,12], evaluated on the plane perpendicular to the loading direction, was adopted as the representative defect size.

Furthermore, each defect was approximated by an equivalent ellipsoid with the same projected area as the actual defect. The semi-axes a, b, and c ($a \geq b \geq c$) were determined as follows:

$$\begin{cases} a = \max\left(\sqrt{\frac{1}{\pi}\frac{\text{area}_{xy}\,\text{area}_{xz}}{\text{area}_{yz}}}, \sqrt{\frac{1}{\pi}\frac{\text{area}_{xy}\,\text{area}_{yz}}{\text{area}_{xz}}}, \sqrt{\frac{1}{\pi}\frac{\text{area}_{xz}\,\text{area}_{yz}}{\text{area}_{xy}}}\right) \\ b = \left(\sqrt{\frac{1}{\pi}\frac{\text{area}_{xy}\,\text{area}_{xz}}{\text{area}_{yz}}}, \sqrt{\frac{1}{\pi}\frac{\text{area}_{xy}\,\text{area}_{yz}}{\text{area}_{xz}}}, \sqrt{\frac{1}{\pi}\frac{\text{area}_{xz}\,\text{area}_{yz}}{\text{area}_{xy}}}\right) \cap \bar{a} \cap \bar{c} \\ c = \min\left(\sqrt{\frac{1}{\pi}\frac{\text{area}_{xy}\,\text{area}_{xz}}{\text{area}_{yz}}}, \sqrt{\frac{1}{\pi}\frac{\text{area}_{xy}\,\text{area}_{yz}}{\text{area}_{xz}}}, \sqrt{\frac{1}{\pi}\frac{\text{area}_{xz}\,\text{area}_{yz}}{\text{area}_{xy}}}\right) \end{cases} \quad (1)$$

where the equivalent ellipsoid preserves the projected area of the defect while providing a simplified geometrical representation suitable for subsequent analyses.

3. Analysis of contour-induced defects

3.1. Spatial distribution and classification

XCT analyses of the fatigue specimens and the bracket revealed significant spatial variations in defect density throughout the volume (Figs. 3 and 4). The colour scale represents the equivalent defect diameter. For each material, the largest detected defect is shown enlarged in Fig. 3.

In particular, a well-defined near-surface layer characterised by elevated defect density was identified in the contouring region of the

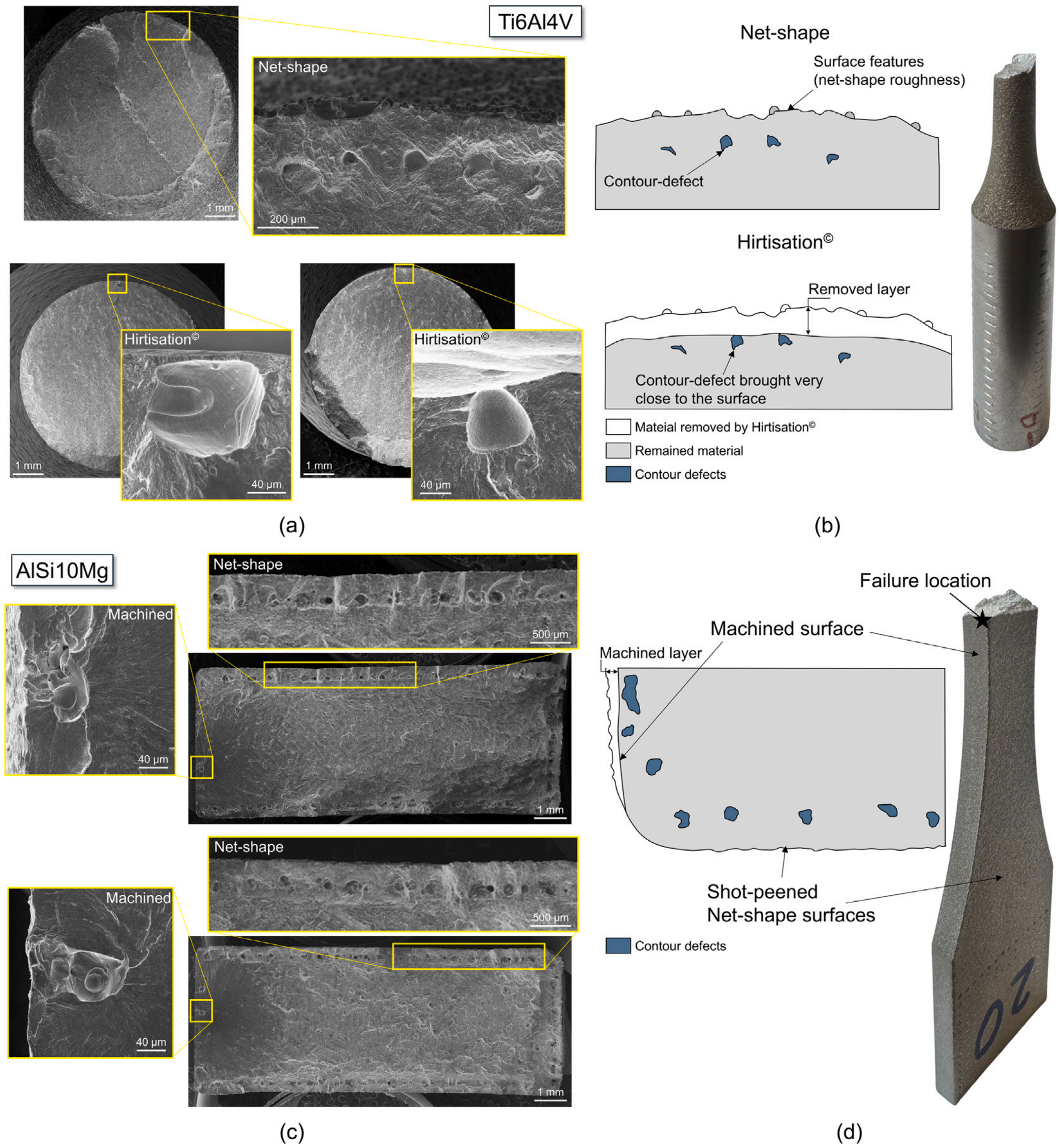

Fig. 1. Fatigue database: (a) Ti6Al4V specimens, showing surface-roughness-induced crack initiation in the net-shape condition and contour-induced critical defects in the Hirtisation® condition; (b) schematic of the Ti6Al4V specimen geometry with a chemically milled surface [38]; (c) AlSi10Mg specimens, showing contour-induced critical defects exposed on the machined surface and on the shot-peened net-shape surfaces; (d) schematic of the AlSi10Mg specimen geometry, indicating the machined surface, the shot-peened net-shape surfaces, and the failure location [39].

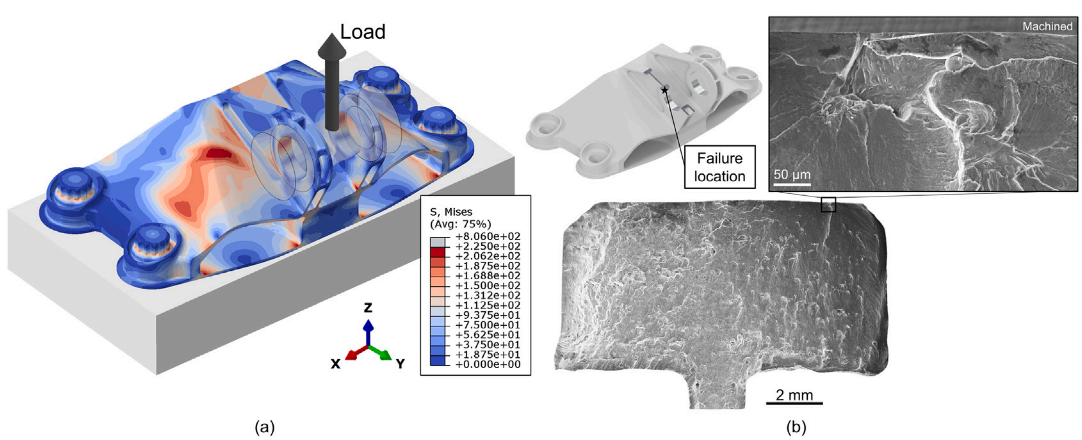

Fig. 2. (a) FE von Mises stress distribution of the bracket under the applied loading condition [62]. (b) Fracture surface of the component showing crack initiation at the lug, in a machined area [39].

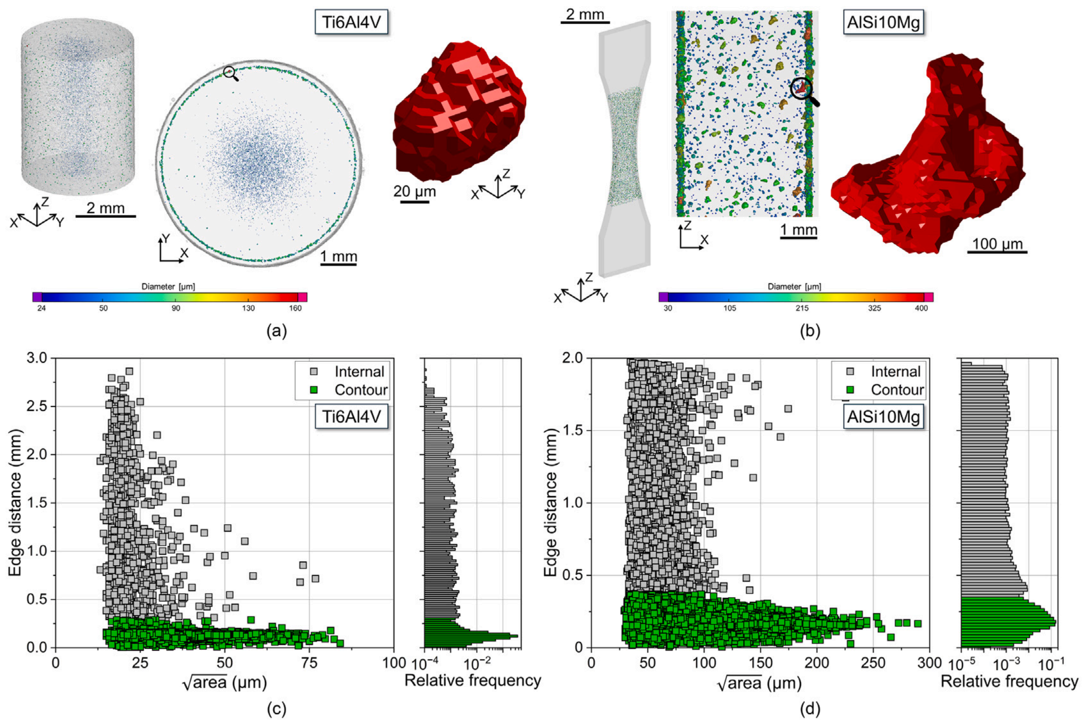

Fig. 3. XCT analysis of defect populations in Ti6Al4V (a,c) and AlSi10Mg (b,d): reconstructed volumes and defect size versus edge distance with corresponding relative frequency distributions.

net-shape surfaces (Fig. 3(a) and (b)), corresponding to the interface between the contour scans and bulk hatching.

The edge-distance analysis of the fatigue specimens shown in Fig. 3(c) and (d) quantitatively confirms this trend. A considerable increase in defect frequency is observed within a confined subsurface layer, whereas defects in the hatch region are more uniformly and sparsely distributed, resulting in a significantly lower density. For the Ti6Al4V specimens, the contouring region exhibits a defect density of approximately 24.7 defects/mm^3, compared with approximately 1.03 defects/mm^3 in the hatch region.

To distinguish contour-induced defects from internal volumetric defects, an edge-distance threshold was introduced. For Ti6Al4V, the contour–hatch transition depth was estimated to be approximately 300 µm below the free surface, whereas for AlSi10Mg the corresponding transition depth was set to 370 µm, consistent with the contour thickness measured from XCT reconstructions.

A further relevant observation concerns the defect size distribution reported in Fig. 3(c) and (d). For both specimens, the larger defects are predominantly located within the contour-dominated layer, indicating that this region hosts not only a higher defect density but also larger defects. Defect morphology ranges from highly irregular shapes to nearly spherical pores, suggesting a process-related origin associated with the contour–hatch transition. Potential mechanisms include insufficient overlap between adjacent scan tracks or local variations in laser energy input, which may promote defect formation [64,65].

As summarised in Table 1, the longitudinal, that is, load-direction, and circumferential, that is, perpendicular to the load-direction, defect distributions are described using a set of key parameters. The linear density ($\rho_{l,l}$ and $\rho_{l,c}$) represents the number of defects per unit length and the average inter-defect spacing ($\bar{d}_{z,l}$ and $\bar{d}_{z,c}$) provides an intuitive measure of the mean distance between defects.

The results highlight a clear difference between the Al and Ti specimens in terms of both density and spacing. The Al specimen exhibits a longitudinal linear defect density of 8.29 defects/mm, corresponding to a mean distance of 120 µm, whereas the Ti specimen shows a lower density of 1.36 defects/mm and a larger mean distance of 740 µm. Consistently, $\bar{d}_{z,l}$ is significantly smaller in the Al specimen, indicating a more closely spaced defect distribution along the loading direction, which may promote interaction between stress fields.

Table 1
Defect distribution parameters for Al and Ti specimens in hatch and contour regions, including volumetric density and longitudinal/circumferential characteristics.

Material	Region	ρ_v	Longitudinal		Circumferential	
		(def./mm^3)	$\rho_{l,l}$ (def./mm^{-1})	$\bar{d}_{z,l}$ (mm)	$\rho_{l,c}$ (def./mm^{-1})	$\bar{d}_{z,c}$ (mm)
Al	Hatch	0.95	–	–	–	–
	Contour	28.9	8.29	0.12	2.51	0.24
Ti	Hatch	1.03	–	–	–	–
	Contour	24.7	1.36	0.74	0.85	1.46

The bracket component (Fig. 4) exhibits a spatial defect distribution consistent with that observed in the Al fatigue specimens (Fig. 3(b) and (d)). The reconstructed volume reveals an heterogeneous spatial distribution of defects, with a pronounced concentration in regions corresponding to net-shape surfaces. The magnified views, regions A and C in Fig. 4, further highlight the preferential accumulation of larger defects within the contour-affected layer adjacent to the free surface. In contrast, the machined surfaces of the component lug, region B in Fig. 4, were subjected to material removal exceeding 1 mm. This machining depth completely eliminated the contour-affected layer, resulting in the absence of contour-induced surface defects in these regions.

As in fatigue specimens, this spatial distribution in the net-shape surfaces confirms the presence of a contour-dominated subsurface region characterised by both increased defect density and larger defect size. In contrast, defects within the bulk hatch region appear more sparsely distributed and generally smaller. The consistency between specimen and component-scale observations indicates that the contouring strategy systematically generates a distinct near-surface defect population, independent of geometrical complexity.

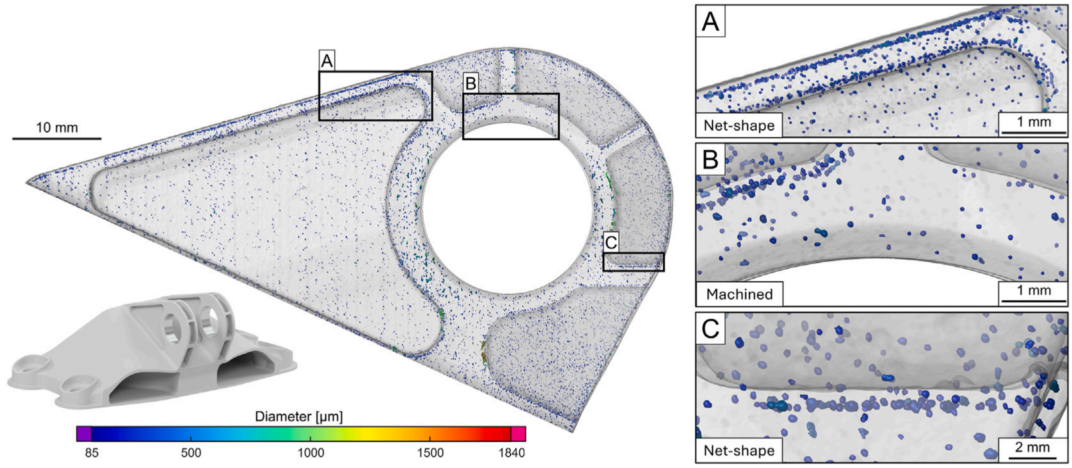

Fig. 4. XCT reconstruction of the bracket component. Magnified regions (A–C) highlight defect localisation in net-shape and machined areas.

This spatial localisation demonstrates that contour-induced defects constitute a distinct defect population characterised by specific spatial and dimensional attributes. These findings provide the physical basis for the subsequent modelling strategy, in which contour-induced defects are treated separately from internal volumetric defects.

3.2. Effect of surface removal on SIF

In AMed components, fatigue performance is largely controlled by process-induced defects, which act as crack initiation sites [1,3,4]. Their assessment is commonly framed within fracture mechanics, based on the assumption that defects can be treated as equivalent cracks, enabling the use of crack propagation and threshold models [8–10].

Within this context, the driving-force metric of fracture mechanics, the Mode I SIF (K), provides a quantitative descriptor of defect severity. Each defect is modelled as an individual crack-like feature, and its SIF is evaluated using analytical solutions for embedded and elliptical surface cracks (Fig. 5). In general, the SIF can be expressed by Eq. (2):

$$K = F \cdot \sigma \cdot \sqrt{\pi \cdot a} \tag{2}$$

where F is the shape factor, σ is the applied stress, and a is the crack size. Defects are idealised as equivalent ellipsoids characterised by semi-axes a, b, and c, as described in Section 2.3. In the adopted reference system, the semi-axes a and b lie in the plane normal to the loading direction, with a parallel to the specimen surface and b oriented along the surface normal.

Depending on their position relative to the free surface and their size, defects can be classified as *internal* or *surface* defects. Commonly adopted criteria classify *surface* defects when their distance from the free surface is below a given threshold, often expressed as a function of defect size parameters such as the semi-axis b, $\sqrt{area}$, or $\sqrt{area}_{eff}$ [66–68].

In this study, Murakami's criterion [66] is adopted. The transition between internal and surface defects is defined in terms of the ratio between the defect semi-axis b and the distance d from the defect centroid to the free surface. Specifically, near-surface defects are classified as *internal* when $b/d \leq 0.8$, and as *surface* defectsotherwise. A comparison with alternative criteria is provided in Section 4.1.

- Internal defects ($b/d \leq 0.8$)
  Defects satisfying this condition are treated as embedded cracks. If the defect is more elongated in the tangential direction with respect to the surface ($b/a \leq 1$), the solution for an *elliptical crack near a free surface* (Fig. 5(a)) proposed by Isida and Noguchi [69] is adopted. In contrast, if the defect is more elongated in the radial direction ($b/a > 1$), the analytical solution for an *elliptical crack in an infinite body* (Fig. 5(b)) originally derived by Irwin [70] is used.
- Surface defects ($b/d > 0.8$)
  In this case, defects are treated as surface-breaking cracks, and the weight function method proposed by Wang and Lambert [71,72] is adopted for semi-elliptical surface cracks. If $b/a \leq 1$, an equivalent surface defect is defined with a depth equal to $h + 2b$ and a width determined by preserving the original aspect ratio of the defect (Fig. 5(c)). If $b/a > 1$, the equivalent surface crack is defined with a depth equal to $h+2b$ and a width equal to $2a$ (Fig. 5(d)). Here, h denotes the edge distance of the defect.

Defects that directly intersect the free surface are treated as surface cracks with their actual geometrical dimensions, and the weight-function method proposed by Wang and Lambert [71,72] is adopted.

The VM procedure specifically accounts for post-processing operations involving material removal (e.g. machining for AlSi10Mg specimens or chemical milling for Ti6Al4V specimens). The procedure numerically removes a prescribed thickness of material from the surface of the XCT dataset, thereby updating the defect-surface distance and may alter defect morphology when the removal process intersects pre-existing defects. As a result, initially internal-contour defects may assume different configurations (Fig. 6(a)):

- remain fully embedded within the material, that is, internal defects;
- become partially intersected by the newly generated surface, that is, surface defects;
- transform into surface-breaking defects, that is, surface defects.

For each defect, the SIF is evaluated at point A, as shown in Fig. 6(a), applying a stress of 1 MPa. When the SIF and the corresponding shape factor are evaluated for the net-shape condition (Fig. 6(b)), contour-induced defects are predominantly classified as internal. In this configuration, their crack-driving force remains lower than that associated with sharp surface irregularities, in agreement with the fractographic observations.

For the Ti6Al4V specimens, the VM procedure was applied by virtually removing a surface layer of 66 μm, corresponding to the material removal achieved experimentally by the Hirtisation® process (Fig. 6(c)). The defect morphology and the distance from the newly generated free surface were consequently updated, and the corresponding SIF was recalculated. The analysis reveals a significant increase in the shape factor for a substantial fraction of defects, consequently resulting in a considerable increase in the SIF, especially for initially subsurface contour-induced defects. Moreover, a non-negligible number of defects transition into the surface-defect regime.

This predicted transition is consistent with the experimental evidence: material removal processes expose pre-existing contour porosity,

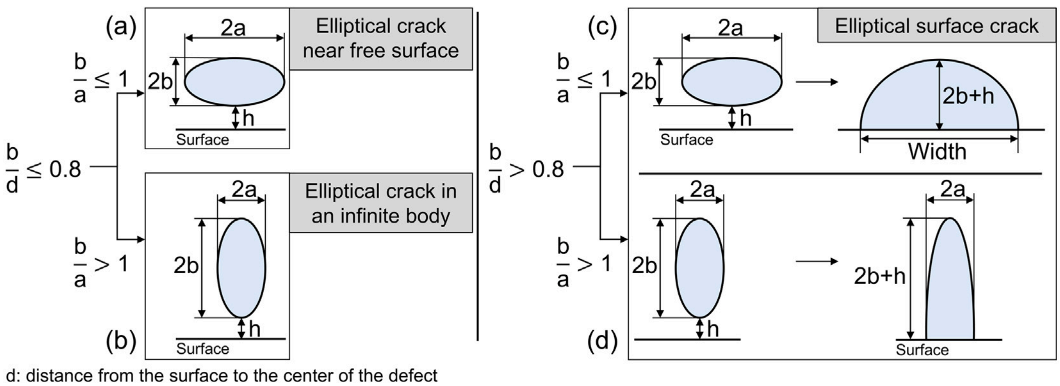

Fig. 5. Schematic representation of the defect configurations and corresponding SIF solutions adopted.

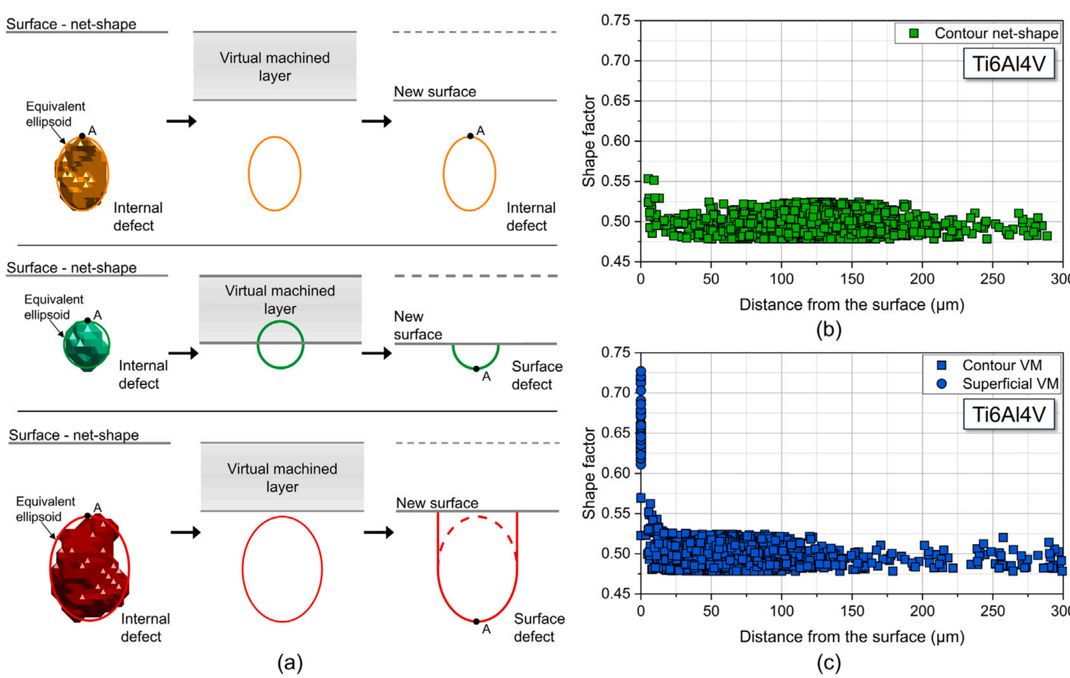

Fig. 6. Application of the VM procedure to contour-induced defects. (a) Schematic representation of the possible defect configurations after material removal. (b) Shape factor as a function of distance from the surface in the net-shape condition. (c) Updated shape factor distribution after VM, showing the transition of a fraction of defects to the surface-defect regime.

increasing the population of surface-breaking defects and thereby shifting the fatigue crack initiation mechanism from superficial roughness features to contour-induced defects.

3.3. Surface defect distribution modelling

Because fatigue failure is controlled by the largest anomalies [73, 74], a dedicated modelling approach is required to provide a statistical description of contour-induced defects, in which defects are treated as individual crack-like features [8–10] and characterised through the corresponding SIF.

The workflow adopted in this study is schematically illustrated in Fig. 7. In the net-shape specimens, the internal contour-defect population is characterised by XCT and subsequent porosity analysis, providing quantitative information on defect size, morphology, and spatial distribution.

When material removal is involved, a VM procedure is employed to numerically reproduce chemical or mechanical material removal, enabling the identification of contour defects interacting with the surface.

Because fatigue failure is governed by the most critical defects, a block maxima (BM) approach is adopted to implement an EVS [75]. The analysed surface is divided into non-overlapping areas, S_o, and, for each area, the maximum SIF of the underlying layer of the contour-induced defects is extracted and classified as originating from either a surface defect or an internal-contour defect. This results in two distinct populations of extreme SIF values.

The extreme SIF values extracted for each S_o are expressed in terms of an equivalent defect size by adopting Murakami's boundary correction factor, $Y = 0.65$ [12], enabling a unified surface-based representation of fatigue-contour defects. To this end, the equivalent defect size, $\sqrt{area}_{eq}$, associated with a given SIF is obtained by inverting Eq. (2), based on the Murakami parameter [11,12], as given in Eq. (3):

$$\sqrt{area}_{eq} = \frac{1}{\pi} \cdot \left(\frac{K}{Y \cdot \sigma} \right)^2 \quad (3)$$

The two populations of $\sqrt{area}_{eq}$, corresponding to surface and internal-contour defects, are independently modelled using a largest

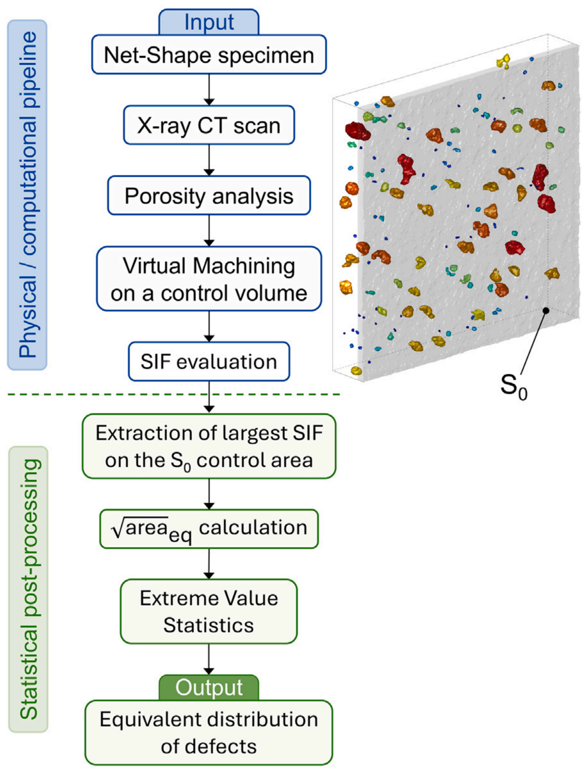

Fig. 7. Overview of the integrated statistical–fracture mechanics workflow for modelling the layer of contour-induced defects.

extreme value distribution (LEVD), whose cumulative distribution function is given by Eq. (4):

$$F(\sqrt{area}_{eq}) = \exp\left[-\exp\left(-\frac{\sqrt{area}_{eq} - \lambda}{\delta}\right)\right] \quad (4)$$

where λ and δ are the location and scale parameters, respectively.

The final defect distribution is obtained by adopting a competing-risk model [76], which accounts for the contributions of surface and internal-contour defects to the fatigue-critical defect population. Assuming statistical independence between the two populations, the resulting cumulative distribution function is given by Eq. (5):

$$F_{tot}(\sqrt{area}_{eq}) = F_{surface}(\sqrt{area}_{eq}) \cdot F_{internal\text{-}contour}(\sqrt{area}_{eq}) \quad (5)$$

If the surface of interest has an area S_c, the corresponding return period is defined by Eq. (6):

$$T = \frac{S_c}{S_o} \quad (6)$$

and the cumulative distribution of the largest defect within S_c is given in Eq. (7):

$$F_{S_c}(\sqrt{area}_{eq}) = [F_{tot}(\sqrt{area}_{eq})]^T \quad (7)$$

3.3.1. Modelling for Ti6Al4V specimens

Fig. 8 shows the application of the proposed statistical workflow to the Ti6Al4V specimens using a reference area of 5 mm^2 for BM sampling after applying the VM procedure to reproduce the experimental Hirtisation® condition (66 μm material removal). As shown in Fig. 8(a), the maximum SIF values extracted from each control area S_o, represented by blue squares in the Gumbel probability plot exhibit a curvilinear trend, indicating the presence of two distinct defect populations. For comparison, the SIF values extracted from the net-shape surface without virtual material removal are also reported in Fig. 8(a) represented by red circles. In this case, the data align along a straight line in the Gumbel probability plot, indicating that they belong to a single population of internal-contour defects. This observation supports the adoption of a competing-risk model based on the combination of two independent LEVDs to describe the VM data. Each population, namely internal-contour defects and surface defects, is independently described by an LEVD according to Eq. (4), and their combination yields the final equivalent defect size distribution representative of the Hirtisation® condition, as shown in Fig. 8(b).

The two populations exhibit markedly different characteristics. The internal-contour defect distribution shows a steeper slope, $\delta = 3.3$ μm, indicating a lower statistical dispersion, whereas the surface-defect distribution extends towards larger equivalent defect sizes ($\delta = 12.7$ μm) and governs the upper tail of the distribution. The resulting combined distribution reflects the contribution of both populations and provides a physically consistent description of the fatigue-critical defects.

To enable direct comparison with experimental observations, the predicted distribution was extrapolated to the reference surface of the specimens, that is, 301.6 mm^2, external surface area of the specimen gauge section, using Eq. (7). The comparison is shown in Fig. 8(c), where the combined distribution is compared with the defect size LEVD obtained from SEM measurements of fatigue-critical defects [38]. Good agreement is observed, demonstrating the capability of the proposed approach to predict both the slope and the values of the experimental distribution.

Table 2
Comparison between the defect size distribution obtained from SEM measurements [38] and the predictions derived from VM for different reference areas used in BM sampling.

Data source	S_0 (mm^2)	$\sqrt{area}_{50\%}$ (μm)	$\sqrt{area}_{97.5\%}$ (μm)
SEM	–	71.9	124.8
VM	5	84	121.6
VM	10	88	131.7
VM	20	86.2	117.8

These observations are further supported by the quantitative comparison reported in Table 2, where the distributions derived for the virtual Hirtisation® condition are compared with the defect size distribution of critical defects obtained from SEM measurements. The predicted $\sqrt{area}_{50\%}$ obtained from VM, 84 to 88 μm, is approximately 20% higher than the SEM-derived value of 71.9 μm, reflecting the fact that the statistical model describes the population of potential fatigue-controlling defects rather than the specific defect that triggered failure. More importantly, the upper-tail percentiles $\sqrt{area}_{97.5\%}$ show close agreement between the VM predictions, 117.8 to 131.7 μm, and the SEM measurements, 124.8 μm. This consistency in the extreme range confirms that the proposed extreme value workflow accurately captures the magnitude of the largest defects governing fatigue initiation. The estimated distribution parameters further show that the location parameter λ increases with the reference area, from 33.4 μm for the smallest reference area of 5 mm^2 to approximately 56.8 μm for 20 mm^2, while the scale parameter δ remains relatively stable, at 9.5–13.2 μm. This indicates a consistent description of the defect population across different sampling areas.

3.3.2. Modelling for AlSi10Mg specimens

Fig. 9 shows the implementation of the developed methodology for the AlSi10Mg specimens to derive defect size distributions for both the net-shape surfaces and the machined-side condition. The latter was obtained after applying the VM procedure to reproduce the experimental machining condition (approximately 100 μm material removal). In Fig. 9(a), the maximum SIF extracted for each $S_o = 4$ mm^2 is reported. The SIF values corresponding to the net-shape surface follow a linear trend, indicating that they belong to a single family of internal-contour defects. In contrast, the SIF values obtained after material removal exhibit

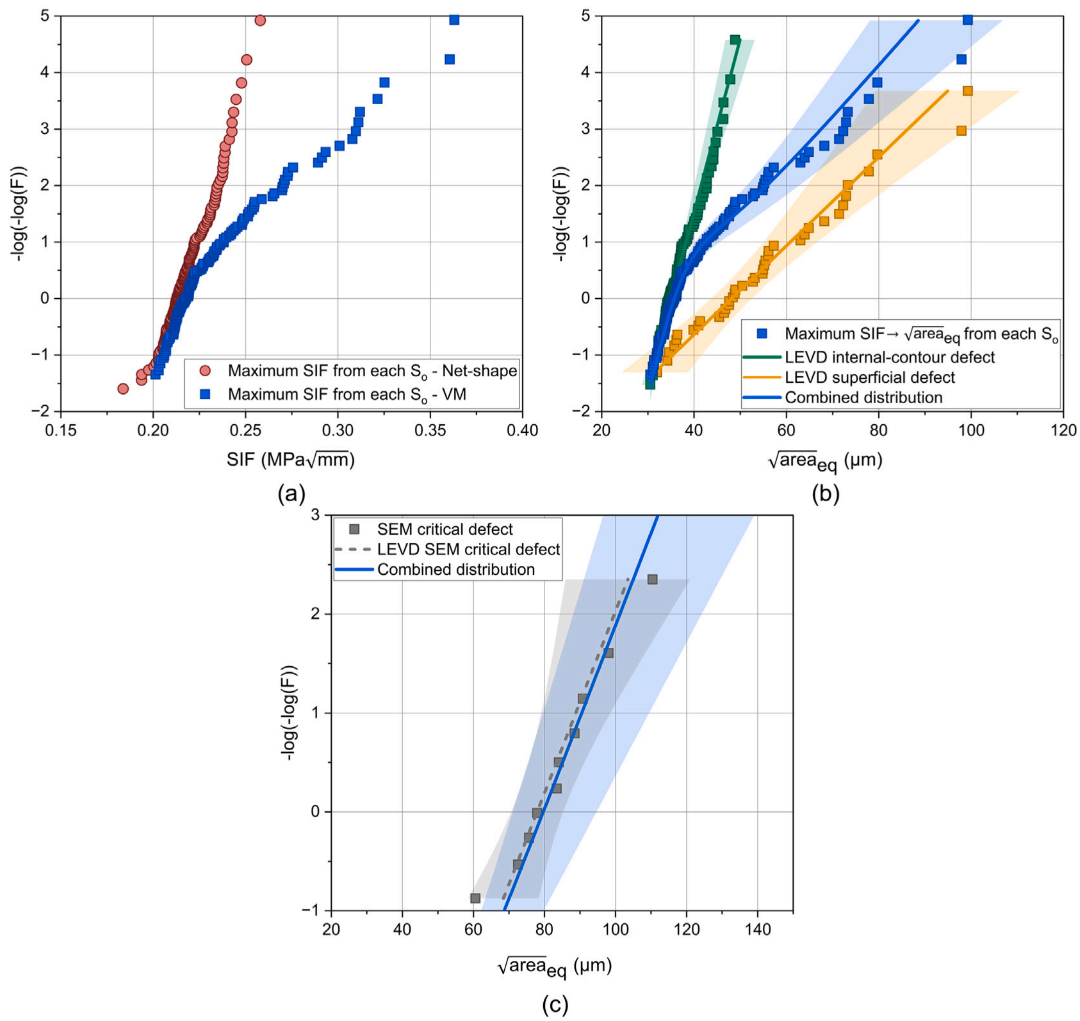

Fig. 8. Statistical modelling of fatigue-critical defects for Ti6Al4V specimens. (a) Maximum SIF values extracted from each control area, under net-shape and VM conditions. (b) LEVDs fitted to the internal- and surface-defect populations identified after VM, together with the combined distribution. (c) Comparison between the predicted distribution, extrapolated to the specimen reference area, and the defect size distribution of fatigue-critical defects measured by SEM.

a curvilinear trend and significantly higher magnitudes, particularly in the upper tail of the distribution, corresponding to defects classified as surface defects. Fig. 9(b) and Table 3 report the distributions and the corresponding values for surface defects in the net-shape surfaces and for the machined side, extrapolated using Eq. (7) to the specimen reference area of 522 mm^2, which corresponds to the region subjected to stresses higher than 90% of the maximum stress. These results are presented together with the defect size distribution derived from SEM observations of the machined side [39].

A significant change in the distribution is observed after machining, primarily reflected by the increase in the scale parameter δ, which rises from 10.2 to 31.7 μm, as shown in Fig. 9(b). This indicates a substantial amplification of the upper tail of the distribution, associated with the increased presence of larger defects. Consistently, $\sqrt{area}_{50\%}$ increases from 151.1 μm for the net-shape condition to 224.3 μm for the machined side, while the upper-tail percentile, $\sqrt{area}_{97.5\%}$, increases from 185.2 to 329.3 μm. The comparison with the SEM data, 246.5 and 394.8 μm, respectively, shows that the VM-based prediction captures the order of magnitude of the defect population observed on the machined side, particularly in the upper tail.

These results indicate that material removal primarily amplifies the upper tail of the distribution by exposing larger contour-induced defects, thereby increasing the population of fatigue-critical surface defects.

Table 3
Comparison between the defect size distribution obtained from SEM observations of the machined surface [39] and the predictions derived from VM for the net-shape and machined conditions.

Surface	S_0 (mm^2)	$\sqrt{area}_{50\%}$ (μm)	$\sqrt{area}_{97.5\%}$ (μm)
Machined side - SEM	–	246.5	394.8
Net-shape	4	151.1	185.2
Machined side - VM	4	224.3	329.3

The VM-based defect distributions are derived from XCT measurements. Although small voxel sizes were employed, the literature indicates that defect-sizing uncertainties may still arise even with small voxel sizes, potentially leading to deviations in the estimated critical defect dimensions [77]. Such measurement uncertainty may partially contribute to the minor shift observed in the predicted distributions.

4. Discussion

4.1. Robustness of the surface defect classification criterion

The classification of defects as internal or surface defects directly influences the evaluation of the SIF and, consequently, the equivalent defect size distribution. In the present study, the transition is

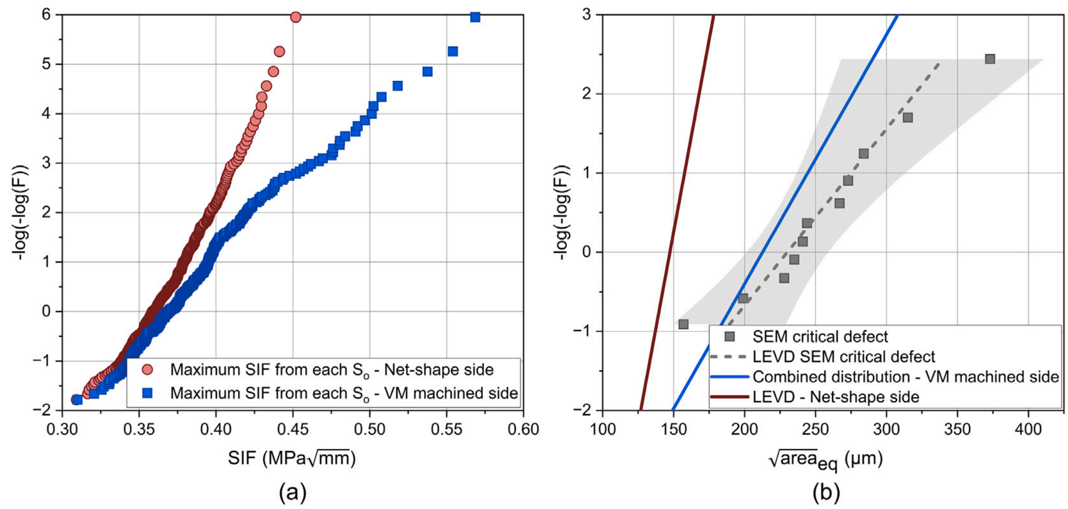

Fig. 9. Statistical modelling of fatigue-critical defects for AlSi10Mg specimens. (a) Maximum SIF values extracted from each control area under net-shape and VM conditions. (b) Comparison of the predicted distributions for net-shape and machined surfaces, extrapolated to the specimen reference area, with the defect size distribution of fatigue-critical defects measured by SEM.

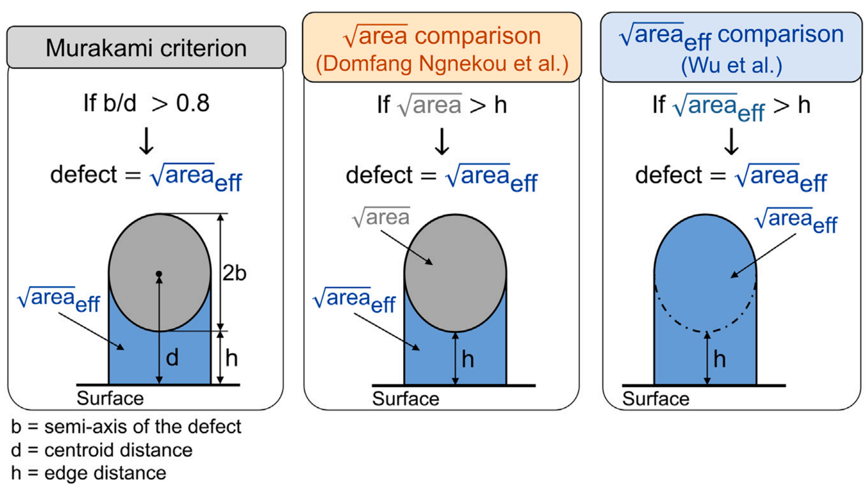

Fig. 10. Schematic comparison of different criteria for the classification of near-surface defects: Murakami-based criterion ($b/d > 0.8$), geometrical criterion based on $h < \sqrt{area}$ [67], and criterion based on the effective defect size $h < \sqrt{area}_{eff}$ [68].

defined according to Murakami's criterion (Fig. 10), based on the ratio $b/d = 0.8$. Other formulations have been proposed to describe the transition between internal and surface defects, generally based on a comparison between a characteristic defect size, $\sqrt{area}$ or $\sqrt{area}_{eff}$, and its distance from the free surface h. In this context, criteria such as $h < \sqrt{area}$ [67] and $h < \sqrt{area}_{eff}$ [68] provide alternative definitions for identifying surface-breaking defects (Fig. 10).

The effect of the defect classification criterion on the equivalent defect size distribution was assessed by considering three alternative definitions for the identification of surface defects: namely the Murakami criterion ($b/d > 0.8$), the geometrical condition $h < \sqrt{area}$, and the effective size-based condition $h < \sqrt{area}_{eff}$.

For each definition, the same procedure was applied: defects were classified as surface or internal defects based on the selected criterion, SIFs were evaluated using the formulations reported in Section 3.2, within their range of validity, and the statistical workflow described in Section 3.3 was used to derive the equivalent defect size distributions.

The results in Table 4 show a marked dependence of the predicted distributions on the adopted definition. For the Ti6Al4V specimens, only the distributions obtained using a reference area, S_0, of 10 mm^2 are reported, and the values for both the Ti6Al4V and AlSi10Mg specimens are extrapolated to the corresponding reference area. In particular, the conditions $h < \sqrt{area}$ and $h < \sqrt{area}_{eff}$ lead to significantly larger defect sizes, both in terms of the $\sqrt{area}_{50\%}$ and $\sqrt{area}_{97.5\%}$ values, because of the increased number of defects classified as surface-breaking. This effect is especially evident in the upper tail of the distribution, which is critical for fatigue strength assessment.

By contrast, Murakami's criterion yields smaller characteristic sizes and shows better agreement with the SEM observations, indicating that restricting the definition of surface defects to those located in close proximity to the free surface provides a more consistent representation of the fatigue-relevant defect population.

These results highlight that the choice of defect classification criterion has a significant impact on SIF evaluation and on the statistical characterisation of defect populations, and must therefore be carefully selected for reliable fatigue predictions.

4.2. Influence of virtual machining depth

The material-removal depth represents a key parameter in the proposed VM procedure. Depending on its value, contour-induced defects may remain subsurface, become exposed at the surface, or be progressively removed (Fig. 6(a)). To investigate its influence, a sensitivity

Table 4
Comparison between SEM and VM defect size distributions.

Source	Criterion	Surface condition	S_0 (mm^2)	$\sqrt{area}_{50\%}$ (μm)	$\sqrt{area}_{97.5\%}$ (μm)
Ti6Al4V – Hirtisation®					
SEM	–	–	–	71.9	124.8
XCT - VM	$b/d > 0.8$	–	10	88.0	131.7
XCT - VM	$h < \sqrt{area}$ [67]	–	10	202.4	325.5
XCT - VM	$h < \sqrt{area}_{eff}$ [68]	–	10	169.4	214.0
AlSi10Mg					
SEM[a]	–	–	–	246.5	394.8
XCT	$b/d > 0.8$	Net-shape	4	151.1	185.2
XCT - VM		Machined side	4	224.3	329.3
XCT	$h < \sqrt{area}$ [67]	Net-shape	4	519.7	698.1
XCT - VM		Machined side	4	396.7	550.3
XCT	$h < \sqrt{area}_{eff}$ [68]	Net-shape	4	460.1	613.4
XCT - VM		Machined side	4	352.8	492.4

[a] All failures occurred on the machined side.

analysis was performed by varying the VM depth for both Ti6Al4V and AlSi10Mg specimens. For each removal depth, the equivalent surface defect distribution was recalculated using the same workflow adopted throughout the study. Fig. 11 shows the values of $\sqrt{area}_{50\%}$ and $\sqrt{area}_{97.5\%}$ for different VM depths, extrapolated to the corresponding specimen reference area.

For both datasets, the equivalent defect distribution is strongly influenced by the amount of removed material. At small removal depths (25-50 μm), only a limited fraction of contour-induced defects is exposed, and the equivalent defect population remains largely controlled by subsurface defects. As the removal depth increases, the VM progressively intersects the region characterised by the highest relative frequency of contour-induced defects (Fig. 11). This region contains the largest statistical population of contour-induced defects available for the extreme value analysis. Consequently, the probability of sampling larger fatigue-controlling defects increases, leading to higher values of $\sqrt{area}_{50\%}$ and $\sqrt{area}_{97.5\%}$. Beyond this region, further material removal progressively eliminates the contour-induced defect population, reducing the number of available defects and leading to a decrease in the equivalent defect size distribution.

Interestingly, the experimentally applied material removal depths (66 μm for Ti6Al4V and 100 μm for AlSi10Mg) lie within the material-removal ranges corresponding to the highest equivalent defect sizes (approximately 50-150 μm for Ti6Al4V and 100-200 μm for AlSi10Mg).

4.3. Validity of the independent defect assumption

The analyses presented so far are based on the assumption that defects behave as isolated cracks in the evaluation of the SIF. However, the defect distribution observed in the contouring region of the AlSi10Mg specimens challenges this assumption. As discussed in Section 3.1, the high linear defect density, $\rho_{l,l} = 8.29$ defects/mm, and the small average spacing, $\bar{d}_{z,l} \approx 120$ μm, indicate that defects are frequently located in close proximity, potentially leading to stress field interactions.

In contrast, the Ti6Al4V specimens exhibit a significantly lower defect density, $\rho_{l,l} = 1.36$ defects/mm, and larger spacing, $\bar{d}_{z,l} \approx 740$ μm, suggesting that defects can reasonably be considered non-interacting. Therefore, interaction effects are expected to be negligible for this material and were not investigated further.

To assess the validity of the isolated-defect assumption in the AlSi10Mg case, stress-field interaction effects between neighbouring contour-induced defects were investigated through FE analyses. Details of the two-dimensional (2D) FE modelling approach, in which the mesh was reconstructed from XCT scans, are provided in Appendix.

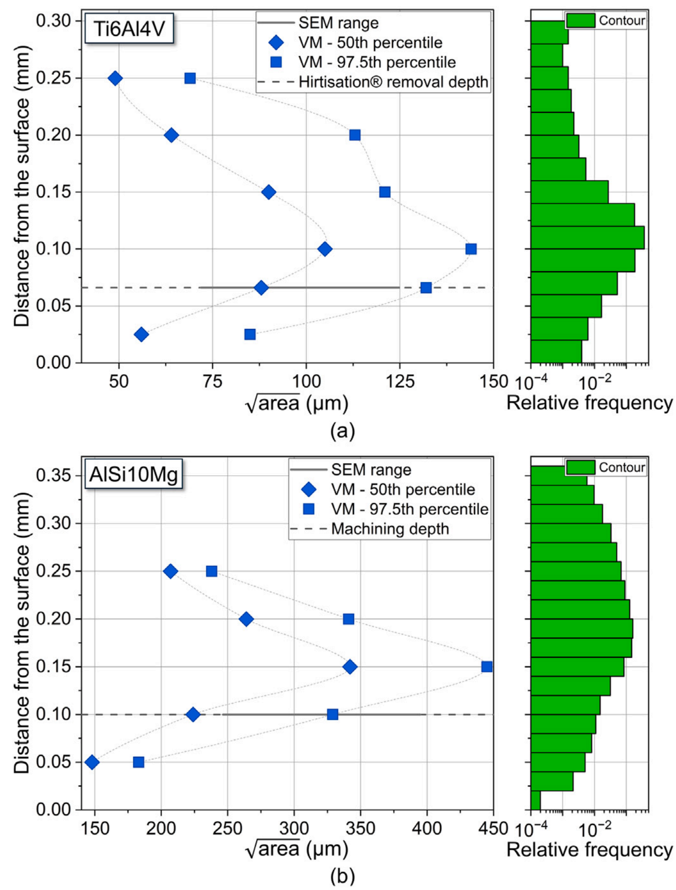

Fig. 11. Distribution of contour-induced defects as a function of the distance from the surface for: (a) Ti6Al4V and (b) AlSi10Mg. Histograms show the relative frequency of contour-induced defects, while markers indicate the 50th and 97.5th percentile defect sizes after VM. Ti6Al4V and AlSi10Mg distributions were derived using sampling areas of 10 mm^2 and 4 mm^2, respectively.

The comparison between the SIF values obtained from neighbouring-defect models and those calculated for the corresponding isolated defects is shown in Fig. 12. The analysed dataset covers an overall length of approximately 125 mm and comprises 200 contour-induced defects, identified through a linear sampling procedure based on 50 sampling windows. The diagonal line represents perfect agreement between the two modelling approaches, while the shaded bands indicate ±10% and ±20% deviations. Fig. 12(b) additionally shows the corresponding relative error, evaluated according to Eq. (8):

$$\text{Relative error} = \frac{K_I^{\text{isolated}} - K_I^{\text{neighbouring}}}{K_I^{\text{isolated}}} \quad (8)$$

Most data points lie within the -10% deviation band, indicating that the neighbouring configuration generally results in a minor reduction in the SIF. The relative error distribution is narrowly centred around zero, with most values on the negative side. The mean shift of approximately −6.5% quantifies this limited shielding effect associated with defect proximity. A limited number of defects, however, exhibit positive values of the relative error, indicating that neighbouring defects may occasionally lead to local stress amplification rather than shielding. Overall, the magnitude of the deviation remains small, confirming that defect interaction has only a minor influence on the local crack driving force. Closer inspection further reveals that the marginally more pronounced shielding effects are mainly associated with defects exhibiting lower SIF values, which are less critical for fatigue. For

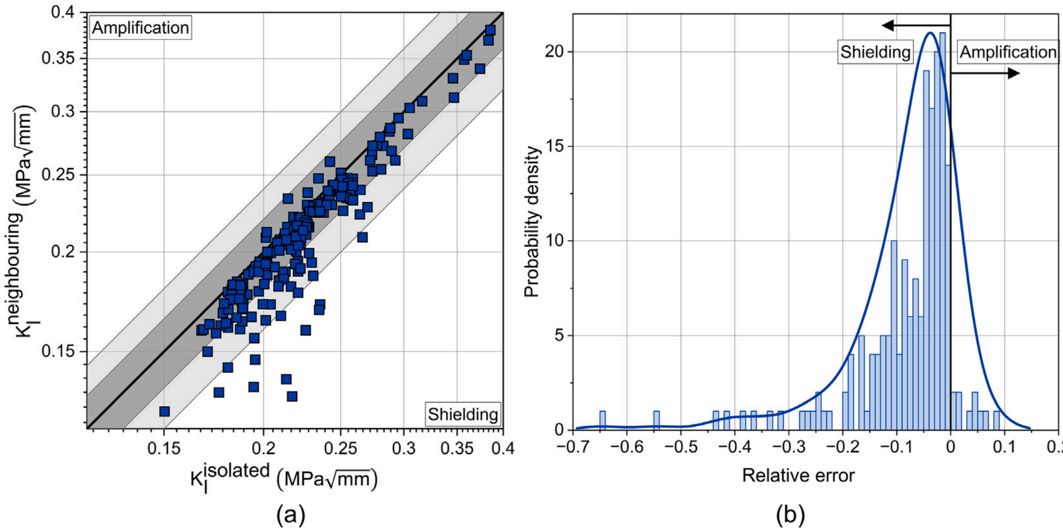

Fig. 12. Mode I SIF comparison between isolated- and neighbouring-defect FE models for 200 contour-induced defects. (a) $K_{I,\text{neighbouring}}$ versus $K_{I,\text{isolated}}$; the diagonal line denotes equality and shaded bands indicate ±10% and ±20% deviations. (b) Probability density of the relative error; negative values indicate shielding, positive values amplification.

defects characterised by higher SIF magnitudes, the interaction effect becomes negligible.

FE modelling has been widely employed to quantify local stress fields around defects, often using XCT-based geometries to capture their morphology [78]. Previous studies have shown that interaction effects between neighbouring defects depend strongly on their relative spacing, orientation and size: defects that are sufficiently far apart behave independently, whereas closely spaced defects may exhibit stress field superposition, leading to shielding or amplification effects [78,79]. However, these analyses are often limited to idealised configurations or a small number of representative defects. In contrast, the present study evaluates interaction effects within neighbouring contour-induced defects directly extracted from XCT data, enabling a statistically meaningful assessment based on a large set of real defect configurations. Shielding effects have also been reported for as-built rough surfaces [80], where interaction between neighbouring surface valleys results in a reduction in the local SIF.

Overall, the results indicate that stress-field interaction effects between neighbouring contour-induced defects are limited for the investigated configurations, supporting the use of the independent-defect assumption as a reliable and computationally efficient approach for fatigue assessment. Within the proposed BM-based statistical workflow, only defects with the highest SIF values are retained as fatigue-controlling defects, inherently reducing the influence of neighbouring defects. Therefore, neglecting shielding effects is consistent with the adopted methodology and leads to a conservative estimation.

5. Application of equivalent defect distribution to life predictions

This section integrates the experimental and numerical results into a probabilistic fatigue assessment framework. Particular attention is devoted to the modelling strategy adopted to account for contour-induced defects and to its implementation within a weakest-link reliability approach. The proposed methodology is first outlined in terms of the computational scheme and subsequently applied to Ti6Al4V and AlSi10Mg specimens and to the bracket component.

5.1. Computational scheme

Probabilistic fatigue assessment frameworks, such as ProFACE [18], DARWIN [20], and P-FAT [81], require a FE model as input to provide the stress state and the geometrical discretisation of the component. The computational implementation of contour-induced defect populations represents a critical aspect of probabilistic fatigue assessment. In zone based probabilistic approaches [82,83], such as those adopted in commercial software, for example, DARWIN [20], the introduction of a contour layer requires explicit partitioning of the FE mesh, as schematically illustrated in Fig. 13(a). A dedicated sub-volume must be created to which a specific defect size distribution is assigned. Although feasible for simple geometries, this strategy becomes impractical when dealing with complex components.

The statistical workflow proposed in this work, described in Section 3.3, enables an alternative implementation. By defining an equivalent surface defect distribution derived from XCT characterisation, contour-induced defects can be treated as a surface population without explicitly partitioning the mesh. In the ProFACE environment [18,84], this allows the direct assignment of the contour-induced defect distribution to the external surface, avoiding the need for geometrical subdivision.

As schematically illustrated in Fig. 13(b), the component is discretised into three regions within the weakest-link framework [55]: (i) a surface layer affected by roughness and contouring, treated as surface cracks with a shape factor of $Y = 0.65$ and shown in red; (ii) an internal volume containing defects characterised by a shape factor of Y=0.65 and shown in green; and (iii) the internal bulk volume containing volumetric defects, with $Y = 0.5$, shown in blue. Each region contributes independently to the overall failure probability according to its associated area or volume.

This implementation significantly enhances modelling flexibility. In particular, it enables the probabilistic assessment of geometrically complex components, such as the investigated bracket, for which explicit mesh partitioning of contour zones would be difficult or even unfeasible.

5.1.1. Probabilistic evaluation of Ti6Al4V specimens

The probabilistic fatigue assessment of the Ti6Al4V specimens was performed using the ProFACE software [18,55], adopting the explicit FCG approach [84]. ProFACE operates as an FE post-processor, extracting stress and volume/area information from the integration points of a prior FE analysis. The FE model provides both the geometrical discretisation and the stress state required by the weakest-link formulation. The sub-volumes and sub-areas are used to evaluate the probability of occurrence of fatigue-critical defects adopting EVS and the corresponding defect size distributions. The stress state is used to determine the

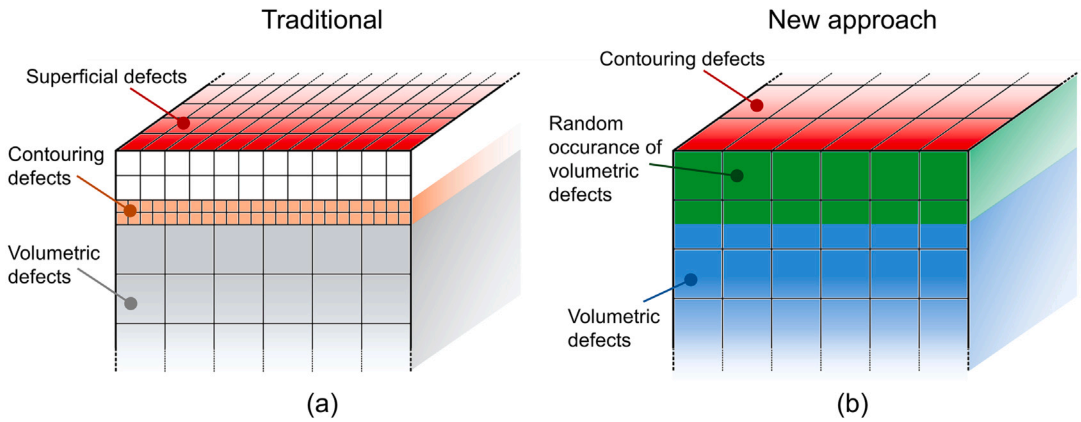

Fig. 13. Comparison between modelling strategies for contour-induced defects. (a) Conventional zone-based scheme with explicit contour-layer partitioning. (b) Proposed surface-equivalent statistical approach implemented in ProFACE, avoiding mesh partitioning.

size of the critical defect associated with the related stress ratio and required number of cycles. Failure probability is evaluated according to weakest-link theory by multiplying the reliability contributions of each sub-volume and sub-area.

In the present study, the material fatigue properties and volumetric defect distribution were adopted from previous investigations [38,84]. The only updated input parameter concerns the modelling of surface-related defects. The FCG analysis was conducted over a representative propagation section of 6 mm × 6 mm, corresponding to the specimen gauge diameter. An average aspect ratio of 1 was assumed for surface anomalies [38].

Two surface-defect configurations were considered. The first was derived from SEM measurements of experimentally observed critical defects [38]. The second was obtained using the statistical workflow proposed in this study, based on XCT-informed contour-layer characterisation and equivalent surface representation. The corresponding LEVD parameters adopted in the life predictions are reported in Table 2.

The probabilistic life predictions obtained using the reference LEVD-based surface distribution and the statistically derived VM-based distributions are compared in Fig. 14. The reference model shows good agreement with the experimental S–N trend and its 95% scatter band.

When the VM-based surface distribution is adopted, the predicted S–N curves exhibit a minor shift towards shorter fatigue lives (Fig. 14(a)). At higher stress levels, for example $\Delta\sigma$ = 820 MPa, (Fig. 14(b)), the LEVD-based model closely matches the experimental data, while the VM implementation yields a marginally more conservative prediction. However, the predicted lives remain within the experimental confidence band. At lower stress levels, for example $\Delta\sigma$ = 580 MPa, (Fig. 14(c)), the LEVD-based model tends to approach the lower bound of the experimental life range. In this regime, the VM-based approach maintains a similar conservative trend without increasing the deviation beyond the observed experimental scatter.

The predicted fatigue life shows limited sensitivity to the adopted reference area within BM sampling, as no significant variations are observed.

5.1.2. Probabilistic evaluation of AlSi10Mg specimens

The probabilistic fatigue assessment of the AlSi10Mg specimens was carried out using ProFACE, adopting the explicit FCG formulation. The crack propagation model was taken from a previously validated benchmark study on PBF-LB AlSi10Mg [55,85]. The residual stress profile implemented in the analysis corresponds to that measured by Rusnati et al. [39], accounting for the effects of the shot peening process and the machined side condition.

In the present simulation, different surface-defect populations (Table 3) were assigned depending on the surface condition. For the three net-shape faces, the contour-induced defect distribution identified from XCT inspections was adopted. For the machined side, the defect population was defined using the proposed VM approach, accounting for contour defects exposed at the surface by material removal. The volumetric defect size distribution for internal defects was obtained using a peak-over-threshold (POT) approach. Only defects with an edge distance greater than 370 μm were considered internal defects (see Fig. 3(d)). A threshold value of 50 μm was adopted, resulting in a negative exponential distribution with a defect density of 0.4795 defects/mm^3 and a scale parameter of 0.0153 μm.

The resulting life predictions are reported in Fig. 15. The ProFACE S–N curve (Fig. 15(a)) shows good agreement with the experimental data and remains within the 95% experimental scatter band. In addition, the normalised failure probability map (Pf norm) in Fig. 15(b) highlights clear localisation of the highest failure probability in the machined surface region.

Notably, the predicted critical region coincides with the experimentally observed crack initiation site, confirming the capability of the proposed modelling framework to correctly identify the governing surface condition. The results therefore demonstrate that the interaction between contour-induced defects and post-processing operations plays a decisive role in controlling fatigue failure in AlSi10Mg specimens, when a thin surface layer is removed.

5.2. Probabilistic evaluation of AlSi10Mg engine bracket component

The probabilistic fatigue assessment was extended to the engine bracket component to evaluate the applicability of the proposed contour-informed workflow to a geometrically complex component. The analysis was performed using ProFACE with the FCG formulation, adopting the same FCG parameters as those used for the AlSi10Mg specimens.

The residual stress state was defined according to the surface condition. In the net-shape regions subjected to shot peening, the residual stress profile previously adopted for the AlSi10Mg specimens was implemented. For the machined surfaces, the residual compressive stress profile reported in [85] for AlSi10Mg machined specimens was considered.

The defect populations assigned to the component were defined consistently with the specimen-scale analysis and surface conditions, as reported in Fig. 16(a). The volumetric defect distribution was assumed to be the same as that described in Section 5.1.2, obtained by applying a POT approach to the volumetric defects of the specimens. For the net-shape surfaces, the contour-induced equivalent surface defect distribution identified from XCT characterisation of the net-shape specimens was adopted.

In the bracket lug, more than 1 mm of material was removed during machining, fully eliminating the contour-affected layer (Fig.

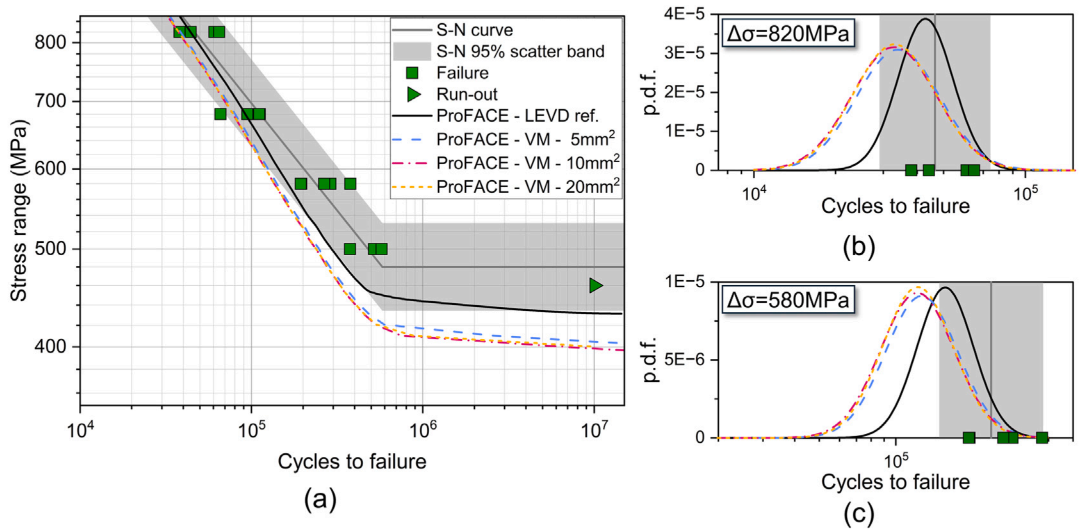

Fig. 14. Probabilistic fatigue life predictions for Ti6Al4V specimens. (a) S–N curves obtained using the reference LEVD-based and VM-based surface distributions, compared with experimental data and the 95% scatter band. (b,c) Corresponding life probability density functions at $\Delta\sigma$ = 820 MPa and $\Delta\sigma$ = 580 MPa.

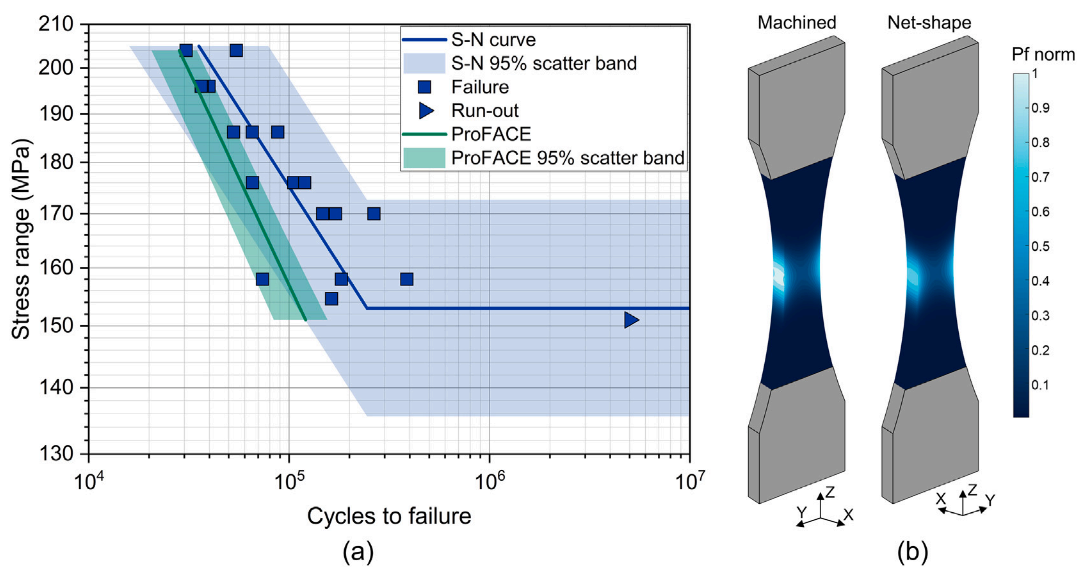

Fig. 15. Probabilistic fatigue assessment of AlSi10Mg specimens. (a) Predicted S–N curve obtained using ProFACE explicit FCG, compared with experimental data and the 95% scatter band. (b) Normalised failure probability map (Pf norm) showing localisation of the critical region in the machined surface.

4). Failure occurred in this region, as shown in Fig. 2(b), and was associated with a lack-of-fusion defect located in close proximity to the machined surface. As a consequence of the machining process, no surface defect distribution was assigned to this region. By adopting the weakest-link framework implemented in ProFACE, the observed failure is inherently captured within the probabilistic formulation. ProFACE discretises the component volume, as shown in Fig. 13(b), accounting for the possibility that volumetric defects may be located near the surface. This is achieved through the definition of a surface volume, calculated analytically as described by Romano et al. [18]. Consequently, contour-induced equivalent surface defects are absent in these regions, and only the occurrence of internal volumetric defects located close to the surface is considered.

The fatigue life predictions obtained for the bracket component are reported in Fig. 16(b), where different defect population assumptions are compared. In particular, three simulations are considered individually: (i) the contribution of contour-induced defects located on the net-shape surfaces; (ii) the contribution associated with the machined surfaces, where the highest stress levels are experienced; and (iii) the overall weakest-link response obtained by accounting for all potential failure locations. The results show that the machined surfaces govern the fatigue failure of the component. The failure probability density associated with the machined condition is shifted towards shorter fatigue lives and matches the experimental number of cycles to failure, indicating that crack initiation is predominantly controlled by the high stress concentration in the machined region of the lug.

The normalised failure probability map shown in Fig. 16(c) further supports this interpretation. The highest $Pf\ norm$ values are observed in the machined region of the lug (region A in Fig. 16(c)), confirming it as the most critical location in agreement with the experimental

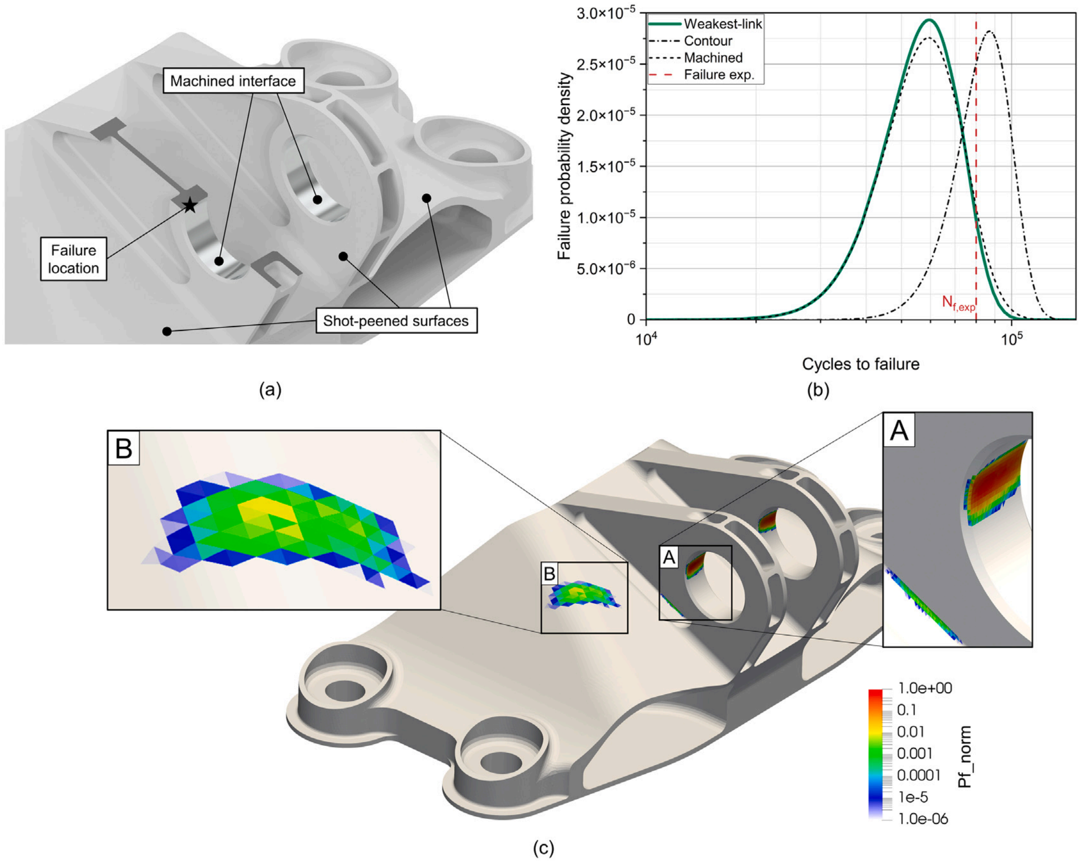

Fig. 16. Probabilistic fatigue assessment of the AlSi10Mg bracket component. (a) Overview of the surface conditions, including the machined interface and shot-peened net-shape surfaces, together with the experimentally observed failure location. (b) Predicted fatigue life distributions considering contour-induced defects on net-shape surfaces, machined surfaces associated with the highest stress levels, and the overall weakest-link response. (c) Normalised failure probability map (Pf norm) showing localisation of the critical region in the machined surfaces.

failure. At the same time, a secondary critical region (region B in Fig. 16(c)) can be identified, where elevated stress levels combine with a non-negligible equivalent surface-defect population arising from contour-induced defects, resulting in a significant local contribution to the overall failure probability. Although contour-induced defects located on the net-shape surfaces are associated with longer fatigue lives than the experimental number of cycles to failure, (Fig. 16(b)), they still represent potentially critical regions, as indicated by their contribution to the $Pf\ norm$ map (region B in Fig. 16(c)). This highlights that, although machined surfaces combined with the highest stresses dominate fatigue failure in the present configuration, net-shape surfaces affected by contour-induced defects may become critical under different loading or geometrical conditions.

The weakest-link prediction, obtained by combining all contributions, provides an accurate description of the experimental fatigue life, showing very good agreement with the experimental cycles to failure. This confirms that the proposed probabilistic workflow is capable of capturing the competing contributions of different surface conditions and correctly identifying the critical regions that control failure.

6. Conclusions

The present study investigated the role of contour-induced defects in controlling the fatigue behaviour of PBF-LB components and addressed the limitations of conventional defect-based approaches in capturing their effects. To this end, a contour-informed XCT-based workflow was developed by combining XCT inspections, VM, and fracture mechanics modelling. The proposed methodology enables the derivation of equivalent surface defect distributions representative of fatigue-critical defects and their direct implementation within a weakest-link fatigue assessment framework, allowing consistent application from the specimen to the component scale.

The following conclusions can be drawn:

- Contour-induced defects form a distinct near-surface population, characterised by both higher density and larger size than bulk defects, and become the dominant fatigue crack initiation sites when exposed at the free surface.
- The VM procedure showed that insufficient material removal does not eliminate contour-induced defects; instead, it promotes their transition into surface-breaking defects, significantly increasing their crack-driving force and contribution to fatigue failure.
- The proposed XCT-based methodology, combining VM and fracture mechanics, enables the derivation of equivalent surface defect distributions that accurately represent fatigue-critical defects, showing good agreement with SEM observations for both Ti6Al4V and AlSi10Mg specimens.
- The contour-informed workflow provides a practical simplification for probabilistic fatigue assessment, as contour-induced defects can be modelled through an equivalent surface defect distribution without explicit mesh partitioning of contour layers.
- The methodology yields accurate fatigue life predictions and correctly identifies failure locations from the specimen to the component scale, demonstrating robust applicability to complex geometries.

CRediT authorship contribution statement

Daniel Perghem: Writing – original draft, Software, Methodology, Investigation, Data curation. **Lorenzo Rusnati:** Visualization, Investigation, Data curation. **Sascha Senck:** Resources, Methodology, Data curation. **Stefano Beretta:** Writing – review & editing, Validation, Supervision, Resources, Formal analysis, Conceptualization.

Declaration of competing interest

The authors declare the following financial interests/personal relationships which may be considered as potential competing interests: Stefano Beretta reports financial support and equipment, drugs, or supplies were provided by European Space Agency. Sascha Senck reports financial support was provided by Austrian Research Promotion Agency. If there are other authors, they declare that they have no known competing financial interests or personal relationships that could have appeared to influence the work reported in this paper.

Acknowledgements

The Ti6Al4V specimens analysed in this study are part of the call-off order of the European Space Agency (ESA/ESTEC) “ESA Additive Manufacturing Benchmarking”, contract number 4000133245 /20/NL/AR/idb. The project involved ESA/ESTEC, The Manufacturing Technology Centre (MTC) and Politecnico di Milano (PoliMi).

The work was supported by the project “sustaiNDT” [grant nr. 909801] via the Austrian Research Promotion Agency (FFG) funded within the framework “Production & Materials” of Austrian Research Promotion Agency (FFG).

Appendix. Investigation of interaction effects in contour defects

Two modelling strategies were adopted to investigate stress-field interactions between defects:

- neighbouring-defect configurations, preserving the relative spatial arrangement observed in the contouring region;
- isolated-defect models, in which each defect was analysed individually.

The comparison between these configurations enabled the assessment of interaction effects on the SIF.

The SIFs of neighbouring contour-induced defects were obtained from FE models directly extracted from XCT reconstructions, as schematically illustrated in Fig. A.17. Neighbouring-defect configurations were identified by selecting defects aligned within planes with normals perpendicular to the loading direction and located at short mutual distances within the contouring region.

The extracted defects were imported into the Sketch module of ABAQUS/CAE to generate two-dimensional FE models. Each defect was approximated as an equivalent ellipse defined by its semi-axes a and c, with c aligned with the loading direction, based on dimensions obtained from the XCT data.

A uniform tensile traction of 1 MPa was applied to the upper edge of the 2D section. Simple support boundary conditions were imposed on the bottom and left edges to prevent rigid body motion.

At the most critical locations of each defect, two-dimensional cracks were introduced perpendicular to the loading direction to evaluate the SIF at point A, as shown in Fig. 6. The crack was modelled with a fixed initial depth of 5 μm ahead of the defect. This value was selected to accurately capture local stress concentration effects. Considering that voxel-level accuracy can be achieved in high-quality XCT inspections, a crack depth close to the voxel size represents a reasonable compromise.

The actual surface roughness was not explicitly modelled. Instead, the external surface was represented by an idealised mean plane, neglecting the geometrical complexity of as-built surface features. Consequently, potential interactions between contour-induced defects and surface roughness, such as sharp valleys, were not considered. Previous studies have shown that such features may act as additional stress concentrators and influence fatigue crack initiation [86]. Therefore, the present analysis is limited to interactions between defects within the material.

The FE mesh consisted of quadratic plane strain elements (CPE8). A refined mesh was adopted in the vicinity of the defects, with further local refinement around the crack tip. Approximately 400 elements

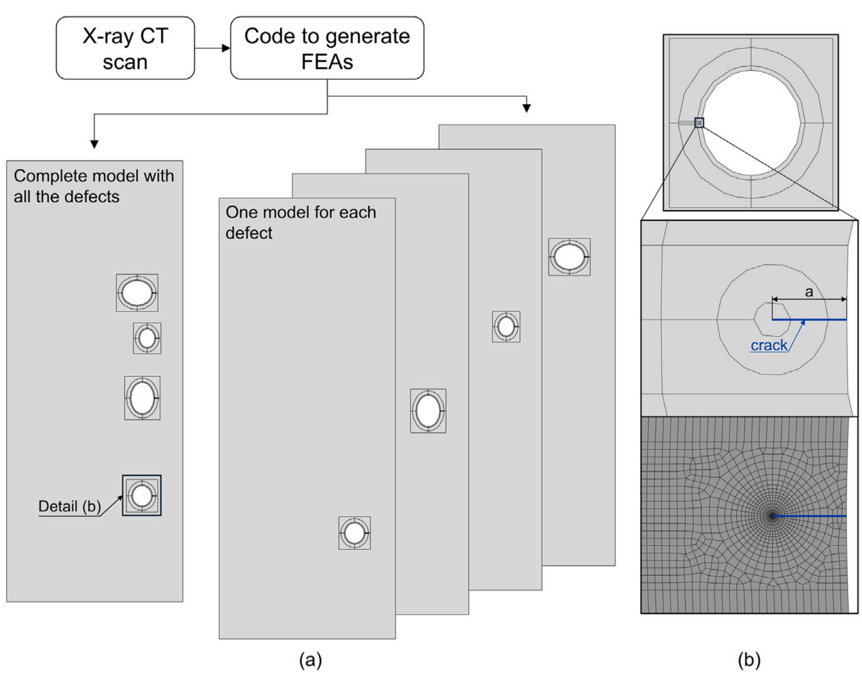

Fig. A.17. (a) Global FE models for neighbouring and isolated defects; the highlighted region indicates the area shown in detail in (b). (b) Zoomed view of the selected region, including crack definition and local mesh refinement.

were used within a circular region of 3 μm diameter surrounding the crack tip to ensure convergence of the SIF results (see Fig. A.17(b)). A static general analysis step was performed. The Mode I SIF was computed using the domain integral (J-integral) method, with 30 contours requested to verify the stability and path independence of the solution.

Data availability

Data will be made available on request.

References

[1] A. Yadollahi, N. Shamsaei, Additive manufacturing of fatigue resistant materials: Challenges and opportunities, Int. J. Fatigue 98 (2017) 14–31, http://dx.doi.org/10.1016/j.ijfatigue.2017.01.001.

[2] H. Javidrad, B. Koc, H. Bayraktar, U. Simsek, K. Gunaydin, Fatigue performance of metal additive manufacturing: a comprehensive overview, Virtual Phys. Prototyp. 19 (1) (2024) http://dx.doi.org/10.1080/17452759.2024.2302556.

[3] N. Sanaei, A. Fatemi, Defects in additive manufactured metals and their effect on fatigue performance: A state-of-the-art review, Prog. Mater. Sci. 117 (2021) 100724, http://dx.doi.org/10.1016/j.pmatsci.2020.100724.

[4] J. Nafar Dastgerdi, M. Lotf Yasouri, H. Remes, Process-induced defects and failure mechanisms in metal additive manufacturing: A mesoscale coupled damage and plasticity modeling and X-ray computed tomography approach, Eng. Fail. Anal. 168 (2025) 109123, http://dx.doi.org/10.1016/j.engfailanal.2024.109123.

[5] J. Berez, L. Sheridan, C. Saldaña, Extreme variation in fatigue: Fatigue life prediction and dependence on build volume location in laser powder bed fusion of 17-4 stainless steel, Int. J. Fatigue 158 (2022) 106737, http://dx.doi.org/10.1016/j.ijfatigue.2022.106737.

[6] C. Chandra, V. Gaur, Fatigue crack initiation in additively manufactured maraging steel: A statistical insight, Int. J. Fatigue 197 (2025) 108957, http://dx.doi.org/10.1016/j.ijfatigue.2025.108957, URL https://www.sciencedirect.com/science/article/pii/S0142112325001549.

[7] A. Mostafaei, C. Zhao, Y. He, S. Reza Ghiaasiaan, B. Shi, S. Shao, N. Shamsaei, Z. Wu, N. Kouraytem, T. Sun, J. Pauza, J.V. Gordon, B. Webler, N.D. Parab, M. Asherloo, Q. Guo, L. Chen, A.D. Rollett, Defects and anomalies in powder bed fusion metal additive manufacturing, Curr. Opin. Solid State Mater. Sci. 26 (2) (2022) 100974, http://dx.doi.org/10.1016/j.cossms.2021.100974.

[8] H. Kitagawa, S. Takahashi, Applicability of fracture mechanics to very small cracks or cracks in the early stage, 1976, pp. 627–631.

[9] M.H. El Haddad, K.N. Smith, T.H. Topper, Fatigue crack propagation of short cracks, J. Eng. Mater. Technol. 101 (1979) 42–46, http://dx.doi.org/10.1115/1.3443647.

[10] J.C. Newman, E.P. Phillips, M.H. Swain, Fatigue-life prediction methodology using small-crack theory, Int. J. Fatigue 21 (1999) 109–119, http://dx.doi.org/10.1016/S0142-1123(98)00058-9.

[11] Y. Murakami, S. Nemat-Nasser, Growth and stability of interacting surface flaws of arbitrary shape, Eng. Fract. Mech. 17 (3) (1983) 193–210, http://dx.doi.org/10.1016/0013-7944(83)90027-9.

[12] Y. Murakami, Metal Fatigue: Effects of Small Defects and Nonmetallic Inclusions, Academic Press, 2019.

[13] M. Chapetti, Fatigue propagation threshold of short cracks under constant amplitude loading, Int. J. Fatigue 25 (2003) 1319–1326, http://dx.doi.org/10.1016/S0142-1123(03)00065-3.

[14] U. Zerbst, M. Madia, D. Hellmann, An analytical fracture mechanics model for estimating of S-N curves of metallic alloys containing large second phase particles, Eng. Fract. Mech. 82 (2012) 115–134, http://dx.doi.org/10.1016/j.engfracmech.2011.12.001.

[15] A. Yadollahi, M. Mahtabi, A. Khalili, H. Doude, J. Newman Jr., Fatigue life prediction of additively manufactured material: Effects of surface roughness, defect size, and shape, Fatigue Fract. Eng. Mater. Struct. 41 (7) (2018) 1602–1614, http://dx.doi.org/10.1111/ffe.12799.

[16] N. Sanaei, A. Fatemi, Defect-based fatigue life prediction of L-PBF additive manufactured metals, Eng. Fract. Mech. 244 (2021) 107541, http://dx.doi.org/10.1016/j.engfracmech.2021.107541.

[17] P. Kishore, T. Singh, R. Aher, A. Alankar, Workflow for fatigue life prediction of additive manufactured complex designs from powder bed fusion of Ti–6Al–4V, Int. J. Fatigue 177 (2023) 107941, http://dx.doi.org/10.1016/j.ijfatigue.2023.107941.

[18] S. Romano, S. Miccoli, S. Beretta, A new FE post-processor for probabilistic fatigue assessment in the presence of defects and its application to AM parts, Int. J. Fatigue 125 (2019) 324–341, http://dx.doi.org/10.1016/j.ijfatigue.2019.04.008.

[19] D. El Khoukhi, F. Morel, N. Saintier, D. Bellett, P. Osmond, V.-D. Le, Probabilistic modeling of the size effect and scatter in High Cycle Fatigue using a Monte-Carlo approach: Role of the defect population in cast aluminum alloys, Int. J. Fatigue 147 (2021) 106177, http://dx.doi.org/10.1016/j.ijfatigue.2021.106177.

[20] Southwest Research Institute, DARWIN Software, 2026, http://darwin.swri.org/. (Accessed 5 March 2026).

[21] T. Tomaszewski, A. Skibicki, Probabilistic prediction of the size effect on the fatigue strength for variable length specimens of selective laser melted 316L stainless steel, Int. J. Fatigue 182 (2024) 108225, http://dx.doi.org/10.1016/j.ijfatigue.2024.108225.

[22] E. Salvati, A. Tognan, L. Laurenti, M. Pelegatti, F. De Bona, A defect-based physics-informed machine learning framework for fatigue finite life prediction in additive manufacturing, Mater. Des. 222 (2022) 111089, http://dx.doi.org/10.1016/j.matdes.2022.111089.

[23] J. Horňas, J. Běhal, P. Homola, S. Senck, M. Holzleitner, N. Godja, Z. Pásztor, B. Hegedüs, R. Doubrava, R.R. užek, L. Petrusová, Modelling fatigue life prediction of additively manufactured Ti-6Al-4V samples using machine learning approach, Int. J. Fatigue 169 (2023) 107483, http://dx.doi.org/10.1016/j.ijfatigue.2022.107483.

[24] E. Maleki, N. Shamsaei, A comprehensive study on the effects of surface post-processing on fatigue performance of additively manufactured AlSi10Mg: An augmented machine learning perspective on experimental observations, Addit. Manuf. 86 (2024) 104179, http://dx.doi.org/10.1016/j.addma.2024.104179.

[25] R. Cunningham, S.P. Narra, C. Montgomery, et al., Synchrotron-based X-ray microtomography characterization of the effect of processing variables on porosity formation in laser power-bed additive manufacturing of Ti-6Al-4V, JOM 69 (2017) 479–484, http://dx.doi.org/10.1007/s11837-016-2234-1.

[26] J. Gockel, L. Sheridan, B. Koerper, B. Whip, The influence of additive manufacturing processing parameters on surface roughness and fatigue life, Int. J. Fatigue 124 (2019) 380–388, http://dx.doi.org/10.1016/j.ijfatigue.2019.03.025.

[27] H. Gong, K. Rafi, H. Gu, T. Starr, B. Stucker, Analysis of defect generation in Ti–6Al–4V parts made using powder bed fusion additive manufacturing processes, Addit. Manuf. 1–4 (2014) 87–98, http://dx.doi.org/10.1016/j.addma.2014.08.002, Inaugural Issue.

[28] Z. Chen, X. Wu, D. Tomus, C.H. Davies, Surface roughness of Selective Laser Melted Ti-6Al-4V alloy components, Addit. Manuf. 21 (2018) 91–103, http://dx.doi.org/10.1016/j.addma.2018.02.009.

[29] Z. Chen, S. Cao, X. Wu, C.H. Davies, 13 - Surface roughness and fatigue properties of selective laser melted Ti–6Al–4V alloy, in: F. Froes, R. Boyer (Eds.), Additive Manufacturing for the Aerospace Industry, Elsevier, 2019, pp. 283–299, http://dx.doi.org/10.1016/B978-0-12-814062-8.00015-7.

[30] P. Karimi, C. Schnur, E. Sadeghi, J. Andersson, Contour design to improve topographical and microstructural characteristics of Alloy 718 manufactured by electron beam-powder bed fusion technique, Addit. Manuf. 32 (2020) 101014, http://dx.doi.org/10.1016/j.addma.2019.101014.

[31] E.B. Glaubitz, J.C. Fox, O.L. Kafka, et al., Contour parameters, melt pool behavior, and surface roughness relationships across laser powder bed fusion platforms and metallic alloys, Int. J. Adv. Manuf. Technol. 136 (2025) 4419–4437, http://dx.doi.org/10.1007/s00170-025-15066-0.

[32] S. Yang, Y. Zhang, R. Juan, Z. Li, J. Wu, S.O. Akinwamide, J. Kuva, R.V. Björkstrand, J. Lian, Effect of building orientation, thickness, and contouring on the microstructure and mechanical properties of AlSi10Mg via laser powder bed fusion, Mater. Sci. Eng.: A 923 (2025) 147685, http://dx.doi.org/10.1016/j.msea.2024.147685.

[33] N.T. Aboulkhair, M. Simonelli, L. Parry, I. Ashcroft, C. Tuck, R. Hague, 3D printing of Aluminium alloys: Additive Manufacturing of Aluminium alloys using selective laser melting, Prog. Mater. Sci. 106 (2019) 100578, http://dx.doi.org/10.1016/j.pmatsci.2019.100578.

[34] E. Beevers, A.D. Brandão, J. Gumpinger, M. Gschweitl, C. Seyfert, P. Hofbauer, T. Rohr, T. Ghidini, Fatigue properties and material characteristics of additively manufactured AlSi10Mg – Effect of the contour parameter on the microstructure, density, residual stress, roughness and mechanical properties, Int. J. Fatigue 117 (2018) 148–162, http://dx.doi.org/10.1016/j.ijfatigue.2018.08.023.

[35] M. Auffray, F. Morel, L. Gallegos Mayorga, E. Pessard, T. Baffie, P. Merot, P. Buttin, Prevailing effect of residual stresses and defects on the fatigue strength of net-shape parts produced with Laser Powder Bed Fusion (L-PBF) 316L stainless steel, Int. J. Fatigue 201 (2025) 109107, http://dx.doi.org/10.1016/j.ijfatigue.2025.109107.

[36] E. Glaubitz, O. Kafka, N. Hrabe, J. Gockel, Stress intensity factor – Life: Improving high cycle fatigue understanding of laser powder bed fusion 316L stainless steel by combining effects of stress, defect size, and defect shape, Int. J. Fatigue 206 (2026) 109454, http://dx.doi.org/10.1016/j.ijfatigue.2025.109454.

[37] F. Concli, R. Gerosa, D. Panzeri, L. Fraccaroli, High and low cycle fatigue properties of selective laser melted AISI 316L and AlSi10Mg, Int. J. Fatigue 177 (2023) 107931, http://dx.doi.org/10.1016/j.ijfatigue.2023.107931.

[38] T. Risposi, L. Rusnati, L. Patriarca, A. Hardaker, D. Luczyniec, S. Beretta, Fatigue of Ti6Al4V manufactured by PBF-LB: A comparison of failure mechanisms between net-shape and electro-chemically milled surface conditions, Eng. Fail. Anal. 172 (2025) 109403, http://dx.doi.org/10.1016/j.engfailanal.2025.109403.

[39] L. Rusnati, M. Yosifov, S. Senck, R. Hubmann, S. Beretta, Anomaly detection by X-ray tomography and probabilistic fatigue assessment of aluminum brackets manufactured by PBF-LB, Mater. Des. 248 (2024) 113467, http://dx.doi.org/10.1016/j.matdes.2024.113467.

[40] E. Maleki, A. Bidar, K. Rahmdel, S. Shao, N. Shamsaei, Laser beam powder bed fused AlSi10Mg: An overview on the effect of post-processing on the microstructure and mechanical properties, Mater. Des. 261 (2026) 115336, http://dx.doi.org/10.1016/j.matdes.2025.115336.

[41] A. Malakizadi, D. Mallipeddi, S. Dadbakhsh, R. M'Saoubi, P. Krajnik, Post-processing of additively manufactured metallic alloys – A review, Int. J. Mach. Tools Manuf. 179 (2022) 103908, http://dx.doi.org/10.1016/j.ijmachtools.2022.103908.

[42] N.E. Uzan, S. Ramati, R. Shneck, N. Frage, O. Yeheskel, On the effect of shot-peening on fatigue resistance of AlSi10Mg specimens fabricated by additive manufacturing using selective laser melting (AM-SLM), Addit. Manuf. 21 (2018) 458–464, http://dx.doi.org/10.1016/j.addma.2018.03.030.

[43] D.A. Lesyk, V.V. Dzhemelinskyi, S. Martinez, et al., Surface shot peening post-processing of inconel 718 alloy parts printed by laser powder bed fusion additive manufacturing, J. Mater. Eng. Perform. 30 (2021) 6982–6995, http://dx.doi.org/10.1007/s11665-021-06103-6, URL https://doi.org/10.1007/s11665-021-06103-6.

[44] E. Maleki, S. Bagherifard, N. Razavi, M. Riccio, M. Bandini, A. du Plessis, F. Berto, M. Guagliano, Fatigue behaviour of notched laser powder bed fusion AlSi10Mg after thermal and mechanical surface post-processing, Mater. Sci. Eng.: A 829 (2022) 142145, http://dx.doi.org/10.1016/j.msea.2021.142145.

[45] S. Romano, P. Nezhadfar, N. Shamsaei, M. Seifi, S. Beretta, High cycle fatigue behavior and life prediction for additively manufactured 17-4 PH stainless steel: Effect of sub-surface porosity and surface roughness, Theor. Appl. Fract. Mech. 106 (2020) 102477, http://dx.doi.org/10.1016/j.tafmec.2020.102477.

[46] D. Greitemeier, C. Dalle Donne, F. Syassen, J. Eufinger, T. Melz, Effect of surface roughness on fatigue performance of additive manufactured Ti–6Al–4V, Mater. Sci. Technol. 32 (7) (2016) 629–634, http://dx.doi.org/10.1179/1743284715Y.0000000053.

[47] A.R. Balachandramurthi, J. Moverare, N. Dixit, R. Pederson, Influence of defects and as-built surface roughness on fatigue properties of additively manufactured Alloy 718, Mater. Sci. Eng.: A 735 (2018) 463–474, http://dx.doi.org/10.1016/j.msea.2018.08.072.

[48] A. Salmi, F. Calignano, M. Galati, E. Atzeni, An integrated design methodology for components produced by laser powder bed fusion (L-PBF) process, Virtual Phys. Prototyp. 13 (3) (2018) 191–202, http://dx.doi.org/10.1080/17452759.2018.1442229.

[49] V. Urlea, V. Brailovski, Electropolishing and electropolishing-related allowances for powder bed selectively laser-melted Ti-6Al-4V alloy components, J. Mater. Process. Technol. 242 (2017) 1–11, http://dx.doi.org/10.1016/j.jmatprotec.2016.11.014.

[50] M. Basha, S. Basha, V. Jain, M. Sankar, State of the art on chemical and electrochemical based finishing processes for additive manufactured features, Addit. Manuf. 58 (2022) 103028, http://dx.doi.org/10.1016/j.addma.2022.103028.

[51] P. Tyagi, T. Goulet, C. Riso, et al., Reducing surface roughness by chemical polishing of additively manufactured 3D printed 316 stainless steel components, Int. J. Adv. Manuf. Technol. 100 (2019) 2895–2900, http://dx.doi.org/10.1007/s00170-018-2890-0.

[52] B. Wysocki, J. Idaszek, J. Buhagiar, K. Szlązak, T. Brynk, K.J. Kurzydłowski, W. Święszkowski, The influence of chemical polishing of titanium scaffolds on their mechanical strength and in-vitro cell response, Mater. Sci. Eng.: C 95 (2019) 428–439, http://dx.doi.org/10.1016/j.msec.2018.04.019.

[53] V. Sandell, J. Nilsson, T. Hansson, P. Åkerfeldt, M.-L. Antti, Effect of chemical post-processing on surfaces and sub-surface defects in electron beam melted Ti-6Al-4V, Mater. Charact. 193 (2022) 112281, http://dx.doi.org/10.1016/j.matchar.2022.112281.

[54] P. Li, D. Warner, N. Phan, Predicting the fatigue performance of an additively manufactured Ti-6Al-4V component from witness coupon behavior, Addit. Manuf. 35 (2020) 101230, http://dx.doi.org/10.1016/j.addma.2020.101230.

[55] F. Sausto, S. Romano, L. Patriarca, S. Miccoli, S. Beretta, Benchmark of a probabilistic fatigue software based on machined and as-built components manufactured in AlSi10Mg by L-PBF, Int. J. Fatigue 165 (2022) 107171, http://dx.doi.org/10.1016/j.ijfatigue.2022.107171.

[56] A. Karolczuk, M. Kurek, M. Ganta, A. Hebda, P. Skubisz, M. gorzata Witkowska, Probabilistic prediction of fatigue life scatter from surface and subsurface defect populations in additively manufactured metals, Addit. Manuf. 124 (2026) 105236, http://dx.doi.org/10.1016/j.addma.2026.105236.

[57] T. Tomaszewski, J. Papuga, Predicting the size-dependent fatigue strength distributions in additively manufactured AlSi10Mg alloy specimens using extreme value statistics, Fatigue Fract. Eng. Mater. Struct. (2026).

[58] I. Holgado, N. Ortega, J.A. Yag00FCe-Fabra, S. Plaza, H. Villarraga-G00F3mez, Metrological evaluation and classification of porosity in metal additive manufacturing using X-ray computed tomography, Mater. Des. 254 (2025) 114057, http://dx.doi.org/10.1016/J.MATDES.2025.114057.

[59] X. Sun, L. Huang, B.G. Xiao, Q. Zhang, J.Q. Li, Y.H. Ding, Q.H. Fang, W. He, H.M. Xie, X-ray computed tomography in metal additive manufacturing: A review on prevention, diagnostic, and prediction of failure, Thin-Walled Struct. 207 (2025) 112736, http://dx.doi.org/10.1016/J.TWS.2024.112736.

[60] M.A. Kurniawan, GE Jet Engine Bracket Version 1.2, 2013, GrabCAD, https://grabcad.com/library/174560. (Accessed 27 March 2026).

[61] S. Senck, M. Happl, M. Reiter, M. Scheerer, M. Kendel, J. Glinz, J. Kastner, Additive manufacturing and non-destructive testing of topology-optimised aluminium components, Nondestruct. Test. Eval. 35 (3) (2020) 315–327, http://dx.doi.org/10.1080/10589759.2020.1774582.

[62] S. Senck, T. Reiter, M. Holzleitner, J. Glinz, J. Kastner, M. Happl, M. Scheerer, Fatigue analysis and non-destructive evaluation of loaded aluminum brackets produced by selective laser melting, in: AIAA SCITECH 2023 Forum, 2023, p. 1670.

[63] S. Senck, S. Rendl, J. Kastner, P. Ehrenfellner, M. Happl, M. Reiter, Simulation-based optimization of microcomputed tomography inspection parameters for topology-optimized aerospace brackets, in: AIAA Scitech 2022 Forum, 2022, p. 0798.

[64] A. Du Plessis, I. Yadroitsava, I. Yadroitsev, Effects of defects on mechanical properties in metal additive manufacturing: A review focusing on X-ray tomography insights, Mater. Des. 187 (2020) 108385.

[65] A.A. Martin, N.P. Calta, S.A. Khairallah, J. Wang, P.J. Depond, A.Y. Fong, V. Thampy, G.M. Guss, A.M. Kiss, K.H. Stone, et al., Dynamics of pore formation during laser powder bed fusion additive manufacturing, Nat. Commun. 10 (1) (2019) 1987.

[66] Y. Murakami, Metal Fatigue: Effects of Small Defects and Nonmetallic Inclusions, Elsevier, Oxford, 2002.

[67] J.N. Domfang Ngnekou, Y. Nadot, G. Henaff, J. Nicolai, W.H. Kan, J.M. Cairney, L. Ridosz, Fatigue properties of AlSi10Mg produced by Additive Layer Manufacturing, Int. J. Fatigue 119 (2019) 160–172, http://dx.doi.org/10.1016/j.ijfatigue.2018.09.029.

[68] Z. Wu, S. Wu, J. Bao, W. Qian, S. Karabal, W. Sun, P.J. Withers, The effect of defect population on the anisotropic fatigue resistance of AlSi10Mg alloy fabricated by laser powder bed fusion, Int. J. Fatigue 151 (2021) 106317, http://dx.doi.org/10.1016/j.ijfatigue.2021.106317.

[69] J.G. Merkle, A Review of Some of the Existing Stress Intensity Factor Solutions for Part-Through Surface Crack, Tech. Rep. ORNL-TM-3983, Oak Ridge National Laboratory, 1973.

[70] G.R. Irwin, Crack-extension force for a part-through crack in a plate, J. Appl. Mech. 29 (1962) 651–654, Trans. ASME, Series E.

[71] X. Wang, S. Lambert, Stress intensity factors for low aspect ratio semi-elliptical surface cracks in finite-thickness plates subjected to nonuniform stresses, Eng. Fract. Mech. 51 (4) (1995) 517–532, http://dx.doi.org/10.1016/0013-7944(94)00311-5.

[72] X. Wang, S. Lambert, Stress intensity factors and weight functions for high aspect ratio semi-elliptical surface cracks in finite-thickness plates, Eng. Fract. Mech. 57 (1) (1997) 13–24, http://dx.doi.org/10.1016/S0013-7944(97)00018-0.

[73] C. Qiu, C. Panwisawas, M. Ward, H.C. Basoalto, J.W. Brooks, M.M. Attallah, On the role of melt flow into the surface structure and porosity development during selective laser melting, Acta Mater. 96 (2015) 72–79, http://dx.doi.org/10.1016/j.actamat.2015.06.004.

[74] A. Tridello, C. Boursier Niutta, M. Rossetto, F. Berto, D. Paolino, Statistical estimation of fatigue design curves from datasets involving failures from defects, Int. J. Fatigue 176 (2023) 107882, http://dx.doi.org/10.1016/j.ijfatigue.2023.107882.

[75] S. Beretta, More than 25 years of extreme value statistics for defects: Fundamentals, historical developments, recent applications, Int. J. Fatigue 151 (2021) 106407, http://dx.doi.org/10.1016/j.ijfatigue.2021.106407.

[76] S. Beretta, C. Anderson, Y. Murakami, Extreme value models for the assessment of steels containing multiple types of inclusion, Acta Mater. 54 (8) (2006) 2277–2289, http://dx.doi.org/10.1016/j.actamat.2006.01.016.

[77] D. Perghem, B. Salehnasab, S. Beretta, S. Shao, N. Shamsaei, ML-based detection of critical defects in additively manufactured parts via X-ray computed tomography, Mater. Des. 260 (2025) 115184, http://dx.doi.org/10.1016/j.matdes.2025.115184.

[78] C.A. Kantzos, R.W. Cunningham, V. Tari, A.D. Rollett, Characterization of metal additive manufacturing surfaces using synchrotron X-ray CT and micromechanical modeling, Comput. Mech. 61 (2018) 575–580, http://dx.doi.org/10.1007/s00466-017-1531-z.

[79] L. Afroz, S.B. Inverarity, M. Qian, M. Easton, R. Das, Analysing the effect of defects on stress concentration and fatigue life of L-PBF AlSi10Mg alloy using finite element modelling, Prog. Addit. Manuf. 9 (2024) 341–359, http://dx.doi.org/10.1007/s40964-023-00457-0.

[80] L. Barricelli, S. Beretta, Analysis of prospective SIF and shielding effect for cylindrical rough surfaces obtained by L-PBF, Eng. Fract. Mech. 256 (2021) 107983.

[81] A. Wormsen, B. Sjödin, G. Härkegård, A. Fjeldstad, Non-local stress approach for fatigue assessment based on weakest-link theory and statistics of extremes, Fatigue Fract. Eng. Mater. Struct. 30 (12) (2007) 1214–1227, http://dx.doi.org/10.1111/j.1460-2695.2007.01190.x.

[82] M. Gorelik, Additive manufacturing in the context of structural integrity, Int. J. Fatigue 94 (2017) 168–177, Fatigue and Fracture Behavior of Additive Manufactured Parts, https://doi.org/10.1016/j.ijfatigue.2016.07.005.

[83] A.M. Park, W.G. Tilson, D.N. Wells, C.G. Lang, C.A. Kantzos, Agency Additive Manufacturing (AM) Certification Support Team (AACT) Risk Reduction–Safe Life Category: Fracture Control Framework for Un-inspectable Fracture Critical AM Parts, Tech. Rep., 2024.

[84] L. Rusnati, G. Minerva, L. Patriarca, S. Miccoli, S. Beretta, Comparison of methods for the determination of fatigue critical flaw size and implementation for probabilistic fatigue assessment, Int. J. Fatigue 203 (2026) 109252, http://dx.doi.org/10.1016/j.ijfatigue.2025.109252.

[85] S. Beretta, L. Patriarca, M. Gargourimotlagh, A. Hardaker, D. Brackett, M. Salimian, J. Gumpinger, T. Ghidini, A benchmark activity on the fatigue life assessment of AlSi10Mg components manufactured by L-PBF, Mater. Des. 218 (2022) 110713, http://dx.doi.org/10.1016/j.matdes.2022.110713.

[86] C. van der Rest, R.A. Manzano Navarrete, A. Simar, O. Poncelet, Influence of roughness and subsurface porosity on the fatigue life of AlSi10Mg produced by Laser Powder Bed Fusion, Mater. Sci. Eng.: A 944 (2025) 148885, http://dx.doi.org/10.1016/j.msea.2025.148885.